OXFORD

Crystal Structure Controls on Oriented Primary Magnetite Micro-Inclusions in Plagioclase From Oceanic Gabbro

Ge Bian [ID][1,*], Olga Ageeva [ID][1,2], Vladimir Roddatis[3], Chen Li[4,5,†], Timothy J. Pennycook[4], Gerlinde Habler [ID][1] and Rainer Abart[1]

[1]Department of Lithospheric Research, University of Vienna, Josef-Holaubek-Platz 2, 1090 Vienna, Austria
[2]Institute of Geology of Ore Deposits, Petrography, Mineralogy, and Geochemistry (IGEM), Staromonetnyi 35, Moscow 119017, Russia
[3]Helmholtz Centre Potsdam, GFZ German Research Centre for Geosciences, Telegrafenberg, D-14473 Potsdam, Germany
[4]Electron Microscopy for Materials Science (EMAT), University of Antwerp, Groenenborgerlaan 171, 2020 Antwerp, Belgium
[5]New address: Thermo Fisher Scientific, Achtseweg Noord 5, 5651 GG Eindhoven, Netherlands

*Corresponding author: Ge Bian, Josef-Holaubek-Platz 2, 1090 Vienna, Austria. Telephone: +43-1-4277-53362. E-mail: biang92@univie.ac.at
†The work included in this manuscript was done in EMAT, Antwerp

Abstract

Oriented needle-, lath- and plate-shaped magnetite micro-inclusions in rock forming plagioclase from mafic intrusive rocks, were investigated using correlated optical microscopy and scanning transmission electron microscopy. The magnetite micro-inclusions were analysed on cuts parallel and perpendicular to the inclusion–elongation directions. The crystal structures of the two phases are in direct contact along the interfaces. The shape, shape orientation and crystallographic orientation relationships between the magnetite micro-inclusions and the plagioclase host appear to be controlled by the tendency of the system to optimise lattice match along the interfaces. The elongation direction of the inclusions ensures good match between prominent oxygen layers in the magnetite and plagioclase crystal structures across the interfaces bounding the inclusions parallel to their elongation direction. In cross-section, additional modes of lattice match, such as the commensurate impingement of magnetite and plagioclase lattice planes along the interfaces, the parallel alignment of the interfaces to low-index lattice planes of magnetite or plagioclase, or the parallel alignment to low index lattice planes of both phases are observed, which appear to control the selection of interface facets, as well as the shape and crystallographic orientation relationships between magnetite micro-inclusions and plagioclase host. The systematics of the inclusion cross-sectional shapes and crystallographic orientation relationships indicate recrystallisation of magnetite with potential implications for natural remanent magnetisation of magnetite-bearing plagioclase grains.

Keywords: scanning transmission electron microscopy, plagioclase hosted magnetite micro-inclusions, interface facets, crystallographic and shape orientation relationships

INTRODUCTION

Oriented magnetite micro-inclusions in rock forming silicate minerals are a common phenomenon in magmatic and metamorphic rocks. Such inclusions often take the form of needles, laths or plates and have been described from olivine (Champness, 1970; Zhang *et al.*, 1999), pyroxene (Fleet *et al.*, 1980; Feinberg *et al.*, 2004; Ageeva *et al.*, 2017) and feldspar (Ageeva *et al.*, 2016; Wenk *et al.*, 2011). In terms of volume, plagioclase is the most abundant mineral in the Earth's crust. Plagioclase from mafic intrusions and their metamorphic derivatives often contains abundant needle-, lath- or plate-shaped magnetite micro-inclusions showing systematic shape orientation relationships (SORs) and crystallographic orientation relationships (CORs) to the plagioclase host (Ageeva *et al.*, 2016, 2020; Sobolev, 1990; Wenk *et al.*, 2011). Based on their elongation directions, two types of magnetite micro-inclusions have been discerned: the first inclusion type has its elongation direction parallel to one of the MT<111> directions, which, in turn, is aligned (sub)parallel to the normal direction of one of seven specific plagioclase lattice planes, including PL(112), PL($\overline{3}$12), PL(150), PL(1$\overline{5}$0), PL(100), PL($\overline{3}$12) and PL(1$\overline{1}$2). According to the classification scheme of Ageeva *et al.* (2020), magnetite inclusions pertaining to this type are referred to as *plane-normal inclusions*. The PL(112), PL($\overline{3}$12), PL(150), PL(1$\overline{5}$0) lattice planes correspond to oxygen layers in the plagioclase crystal structure with nearly identical *d*-spacing as MT{222}, which corresponds to close-packed oxygen layers in the crystal structure of magnetite. Accordingly, the SORs and CORs of the plane-normal type inclusions have been ascribed to the nearly coherent alignment of the close-packed oxygen planes parallel to MT{222} and the corresponding oxygen layers in plagioclase (Ageeva *et al.*, 2020; Bian *et al.*, 2021). This parallel alignment leaves one degree of freedom for rotation about the inclusion elongation direction, giving rise to several CORs within each orientation class. When, apart from the alignment of MT{222} with one of the abovementioned specific PL(*hkl*) lattice planes, no additional rational crystallographic correspondence is found between magnetite and plagioclase, the inclusion is said to have *general orientation* within the respective orientation class. When,

apart from the parallel alignment of MT{222} and a specific PL(*hkl*) lattice plane, a second crystallographic alignment between the lattices of magnetite and plagioclase exists, the inclusion is said to have a specific orientation within the respective PL(*hkl*)-n orientation class (Ageeva *et al.*, 2020). Two specific orientations have been discerned within the respective orientation class. When one of the MT<001> directions is aligned parallel to either PL [14, 10, 7] or the PL [−14, 10, −7] direction, the inclusion is classified as being in *nucleation orientation*. This crystallographic correspondence ensures that FeO_6 octahedra, a building block of crystal structure of magnetite can be accommodated in the channels, formed by six-member rings of AlO_4–SiO_4 tetrahedra and running parallel to PL[001] in the crystal structure of plagioclase. When, instead, one of the MT{220} lattice planes is aligned parallel to a second of the specific lattice planes of plagioclase, the inclusion is classified as being in *main orientation* (see Ageeva *et al.*, 2020).

The second basic type of magnetite micro-inclusions has its elongation direction parallel to MT<110> || PL[001] and is referred to as *PL[001] inclusions*. Several orientation variants related by rotations about the inclusion elongation direction exist also for this inclusion type. Apart from the needle-, lath- and plate-shaped magnetite micro-inclusions, small magnetite micro-inclusions with equant shapes may be present. These inclusions are referred to as *dust-like inclusions*, which also show systematic CORs to the plagioclase host. The plane–normal inclusions supposedly formed by precipitation from primary magmatic Fe-bearing plagioclase, which became supersaturated with respect to magnetite due to cooling or due to changes in oxygen fugacity (Bian *et al.*, 2021). In contrast, most of the PL[001] inclusions appear to have formed during late magmatic, hydrothermal or metamorphic stages.

Magnetite is the most important carrier of the natural remanent magnetisation of rocks, and magnetite-bearing grains of silicate minerals have been investigated intensively due to their significance for paleomagnetic reconstructions (Dunlop & Özdemir, 2001; Nikolaisen *et al.*, 2020, 2022). Ageeva *et al.* (2022) showed that the shape preferred orientation of needle- and lath-shaped magnetite micro-inclusions in plagioclase leads to pronounced anisotropy of the magnetic remanence of magnetite bearing plagioclase grains. As a consequence, the magnetic memory of magnetite bearing plagioclase may be biased, and the direction of the vector of remanent magnetisation may deviate from the direction of the magnetic field at the time, when the rock cooled through the Curie temperature. Understanding the factors controlling the SORs and CORs of needle-, lath- and plate-shaped magnetite micro-inclusions in plagioclase is thus of key importance for paleomagnetic reconstructions, in particular, when single grain methods are applied (Tarduno *et al.*, 2006).

In this paper, we report on high-resolution scanning transmission electron microscopy (HR STEM), as well as on integrated differential phase contrast scanning transmission electron microscopy (iDPC-STEM) of magnetite–plagioclase interfaces from representative inclusions of the plane-normal type. Magnetite–plagioclase interfaces were cut both along and perpendicular to the inclusion elongation directions. The magnetite–plagioclase interfaces are more complex than previously thought. The factors controlling the SORs and CORs of different types of plane-normal inclusions and possible evolution paths are discussed based on the microscopic configuration of the magnetite–plagioclase interfaces. Our findings bear potentially important implications for paleomagnetic reconstructions.

SAMPLE MATERIAL AND ANALYTICAL METHODS
Sample material
Gabbro samples dredged from the mid-Atlantic ridge (MAR) during the 30th cruise of the Research Vessel Professor Logachev (Beltenev *et al.*, 2007; Beltenev *et al.*, 2009; Cipriani *et al.*, 2009) were studied. The dredge sites were within oceanic core complexes at 13°N in the footwalls of a low-angle, large-offset extensional fault, a structural feature, which is typical for slow-spreading ridges (Karson & Lawrence, 1997; MacLeod *et al.*, 2009). More information on the geology of the oceanic core complexes at 13°N can be found in (MacLeod *et al.*, 2009; Ondréas *et al.*, 2012; Pertsev *et al.*, 2012; Escartín *et al.*, 2017). The studied specimens are from gabbroic intrusions in peridotite.

Representative plagioclase hosted magnetite micro-inclusions selected based on magnetite–plagioclase CORs obtained in an earlier electron backscattered diffraction (EBSD) study by Ageeva *et al.* (2020) were investigated. For detailed information on the EBSD method, the reader is referred to these latter authors. The SORs between the magnetite micro-inclusions and the plagioclase host were obtained by combining scanning electron microscopy (SEM) with light-optical polarisation microscopy. The orientations of the facets bounding the magnetite micro-inclusions were reconstructed from known inclusion elongation directions as determined by universal stage measurements under the polarisation microscope combined with the lattice orientations of plagioclase and magnetite as obtained from EBSD (Ageeva *et al.*, 2020).

Focused Ion Beam-SEM and Ar ion-milling
Four specimens were prepared for transmission electron microscopy (TEM) analyses using the focused ion beam (FIB) technique. An FEI Quanta 3D FEG-SEM with integrated FIB device, located at the faculty of Earth Sciences, Geography and Astronomy, University of Vienna, Austria was used. The instrument is equipped with a Schottky field-emission electron gun and a liquid Ga-ion source, a gas injection system for Pt- and C deposition, and an Omniprobe 100.7 micromanipulator for in situ specimen lift-out. The inclusions for TEM studies were selected from chemo-mechanically polished carbon-coated thin sections based on shape orientation obtained from optical microscopy and crystallographic orientation obtained from EBSD analysis, using the same instrument as that for FIB preparation. The first TEM foil contains two needle-shaped PL($\bar{3}$12)n-MT micro-inclusions, one in nucleation and the other in main orientation. The FIB foil was cut perpendicular to the elongation directions of the inclusions and, hence, the cross-sections of the two inclusions were captured in the plane of the FIB foil. The second TEM foil contains a plate-shaped PL($\bar{3}$12)n-MT micro-inclusion in main orientation. The specimen was extracted so that the PL($\bar{3}$12) plane normal lies in the plane of the foil and the plate surface is perpendicular to the plane of the foil. The third TEM foil contains a needle-shaped PL(112)n-MT micro-inclusion in main orientation. The specimen was extracted so that the PL(112) plane normal lies in the plane of the foil. The fourth TEM foil contains the cross-section of the same PL(112)n-MT micro-inclusion as the third foil, and the needle elongation direction is perpendicular to the plane of the foil. Secondary electron (SE) imaging was employed during FIB extraction for monitoring the milling progress. The electron beam was set to 15 kV accelerating voltage and 50 pA probe current. Platinum deposition was used to protect and support the TEM foils during milling, as well as to mount the foil

temporarily to the tip of the tungsten micromanipulator needle and finally to the molybdenum grid. The foils were extracted using an ion beam accelerating voltage of 30 kV, and a probe current that was successively decreased from 65 to 5 nA. The foils for lift-out were about 20×20 microns in area and about 2 to 2.5 microns in thickness. After extraction, the foils were attached to individual Mo grids. For the first three TEM foils, final thinning was done using an accelerating voltage 30 kV, and the probe current was gradually decreased from 1 to 0.03 nA. Finally, FIB low-kV cleaning steps were performed at 5 kV/48 nA and 2 kV/27 pA. The first three TEM foils have a thickness of 30 to 50 nm.

The second, third and fourth TEM specimens were further thinned with a Gatan DuoMill 600 ion mill using argon ions (Ar^+) accelerated through 1 kV and with an incident angle of 15°. Milling was done for about 1 hour from each side. The final thickness of the samples is $\sim$50 nm.

Scanning transmission electron microscopy

STEM was performed on a Thermo Fisher Scientific Themis Z at University of Antwerp. The microscope is equipped with a X-FEG electron source and a monochromator. For imaging, the instrument was operated at 200 kV with a beam current of 5 pA for low-dose exposure. A convergence semi-angle of 20 mrad was used. Bright field (BF) and high-angle annular dark field (HAADF) STEM imaging was done on a needle-shaped PL($\overline{3}$12)n-MT micro-inclusion in nucleation and in main orientation perpendicular to their elongation directions, respectively.

STEM imaging with an integrated differential phase contrast (iDPC) detector was performed at 300 kV with a 10 pA probe current on a Thermo Fisher Scientific Themis Z at the Helmholtz Centre Potsdam, German Research Centre for Geosciences (GFZ-PISA) facility, Potsdam. The microscope is equipped with a X-FEG electron source with a monochromator (energy resolution is <0.3 eV) and with a Cs S-CORR Probe Corrector (80–300 kV). The spatial resolution is <0.06 nm at 300 kV. iDPC-STEM is a relatively novel electron microscopy technique, which allows for imaging light and heavy elements simultaneously at sub-Å resolution with a low-dose incident beam. This is an annular dark field (ADF) technique where a detector consisting of four segments is used, and the iDPC-STEM image contrast is approximately proportional to the atomic number Z in contrast to a power of 1.7 for the HAADF or ADF images collected with a single detector (Bosch & Lazić, 2015; Lazić *et al.*, 2016; Yücelen *et al.*, 2018). High resolution chemical analysis was performed with a SuperX energy dispersive X-ray spectroscopy (EDS) system installed on the Themis Z STEM in Potsdam. HAADF- and iDPC-STEM imaging, as well as chemical analyses were performed on a plate-shaped PL($\overline{3}$12)n-MT micro-inclusion along its elongation direction, and a needle-shaped PL(112)n-MT micro-inclusion along and perpendicular to its elongation direction, respectively.

RESULTS
Mineralogy and petrography

The investigated samples are from gabbro intrusions in peridotites from a mid ocean ridge environment. Plagioclase with anorthite contents of 40 to 60 mol % makes up about 50% by volume of the rock. Apart from plagioclase, clinopyroxene, orthopyroxene and amphibole are present as the main rock forming minerals. The chemical composition of plagioclase in the studied grains has been reported in Ageeva *et al.* (2020, 2022) and is included in the supplementary material I. The investigated

Table 1: Chemical compositions of the plagioclase reported in Wenk *et al.* (1980) from Surtsey, and the plagioclase in the current study

|	Wenk *et al.* (1980)	Plagioclase in the current study
Weight percent oxides		
SiO_2	53.29	54.29
Al_2O_3	30.90	28.58
CaO	13.11	10.93
Na_2O	3.51	5.13
K_2O	0.11	0.16
Fe_2O_3	0.36	0.39
Atoms per formula unit based on 8 oxygens		
Si	2.38	2.46
Al	1.63	1.53
Ca	0.63	0.53
Na	0.304	0.45
K	0.006	0.01
Fe	0.014	0.01

plagioclase has labradorite composition with an overall compositional variability of about 10 mol %. Labradorite has a triclinic crystal symmetry [C-1]. In the following, the crystal structure of labradorite (An62-An66) given by Wenk *et al.* (1980) with lattice constants $a = 8.1736$ Å, $b = 12.8736$ Å, $c = 7.1022$ Å, $\alpha = 93.462°, \beta = 116.054°, \gamma = 90.475°$ was used. The variation of d-spacings and angular relations is minute over the observed 10 mol % compositional variation. The chemical composition of the plagioclase reported in Wenk *et al.* (1980) and the plagioclase in our study are shown in Table 1.

In the petrographic thin section, oriented needle-, lath- and plate-shaped opaque inclusions can be discerned in plagioclase. Based on chemical composition and cubic symmetry, these inclusions were identified as magnetite containing lamellar or irregularly shaped domains of ilmenite and/or ulvospinel. These inclusions likely first formed as titanomagnetite within the plagioclase host, and exsolved into magnetite matrix with ilmenite and/or ulvospinel precipitates (Tan *et al.*, 2016; Gao *et al.*, 2019) in a second phase. A transmitted light plane polarised optical image of a plagioclase grain with oriented magnetite micro-inclusions is shown in Fig. 1. The plagioclase grain is twinned after the pericline twin law. The crystallographic orientation of twin domain 1 is shown in the inserted stereographic projection. Several of the plagioclase plane normal directions and the PL[001] direction, which all correspond to magnetite needle elongation directions, are shown. Based on their shape orientation parallel to the specific plagioclase plane normal directions, abundant needle-shaped PL(112)n-MT, PL($\overline{3}$12)n-MT, PL(100)n-MT and rare PL(150)n-MT micro-inclusions can be discerned in Fig. 1. In addition, PL[001] inclusions and a few plate-shaped magnetite inclusions are present. The edges of the plate-shaped magnetite inclusions follow specific crystallographic directions. For example, the edges trending from upper right to lower left are parallel to the PL($\overline{3}$12)-n direction, the nearly horizontal edges are parallel to one of the MT<111> directions.

Needle-shaped PL($\overline{3}$12)n-MT micro-inclusions

PL($\overline{3}$12)n-MT micro-inclusions have one of their MT<111> directions, the one that is parallel to the inclusion elongation direction, aligned parallel to the normal direction of the PL($\overline{3}$12) plane. As with all plane-normal inclusion types, general and specific
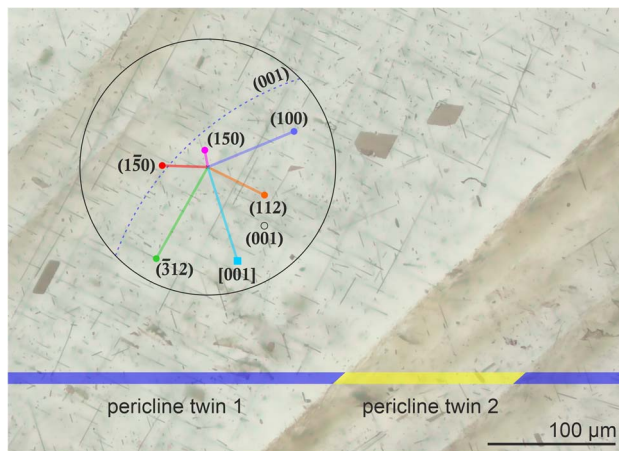
Fig. 1. Transmitted light plane polarised optical photomicrograph of pericline twinned plagioclase with needle-, lath- and plate-shaped magnetite micro-inclusions. The stereographic projection (upper hemisphere) refers to the crystallographic orientation of twin domain 1 and shows the PL(112)n, PL(150)n, PL($\overline{3}$12)n, PL(1$\overline{5}$0)n, PL(100)n as well as the PL[001] direction as colored lines. The plane normal directions correspond to the elongation directions of the needle-shaped magnetite micro-inclusions. The dashed circle indicates the trace of the PL(001) lattice plane, which is the twin plane.

orientation variants are discerned. Among the specific orientation variants, the nucleation orientation, defined by PL($\overline{3}$12)n ∥ MT[111], PL[14,-10,7] ∥ MT[100] and the main orientation, defined by PL($\overline{3}$12)n ∼∥ MT[111] and PL(150) ∥ MT($\overline{2}$02), are the most common (Ageeva *et al.*, 2020). Needle-shaped PL($\overline{3}$12)n-MT micro-inclusions often exhibit about equal proportions of the two orientation variants within one plagioclase grain. Cross-sections of PL($\overline{3}$12)n-MT needles pertaining to either one of the two orientation variants were extracted using FIB. Standard HAADF STEM images of the two cross-sections are shown in Fig. 2a and d. The cross-section of the inclusion in nucleation orientation has a nearly hexagonal shape and is outwards convex all along its perimeter (Fig. 2a). By contrast, the inclusion in main orientation has a nearly rectangular cross-section with a re-entrant section along its perimeter (Fig. 2d). Specific Miller indices are applied for describing the CORs of the different plane-normal inclusion types. The conventions used for assigning specific Miller indices are listed in Table 2. The magnetite micro-inclusion in nucleation orientation has its elongation direction parallel to PL($\overline{3}$12)-n ∥ MT[111]. In addition, the COR is characterised by PL[14,-10,7] ∥ MT[100]. In contrast, the PL($\overline{3}$12)-n magnetite micro-inclusion in main orientation has its elongation direction parallel to PL[$\overline{5}$12] ∥ MT[111], which deviates by about 5° from the PL($\overline{3}$12)-normal direction. In addition, a second parallel alignment of low-index lattice planes, namely PL(150) ∥ MT($\overline{2}$02), holds. The CORs for PL($\overline{3}$12)n-MT micro-inclusions in nucleation orientation and in main orientation are illustrated in Fig. 2b–c and e–f, respectively. The stereographic projections follow the same orientation references as in Fig. 2a and d. Electron diffraction patterns for both cases can be found in the supplementary material II Fig. S1-S2. The nucleation and main orientations are related by a two-step rotation of the lattice of magnetite relative to the lattice of plagioclase: (i) starting from a PL($\overline{3}$12)n-MT micro-inclusions in main orientation a ∼5° rotation of PL about PL(150)n makes PL($\overline{3}$12)n parallel to MT[111] (compare Fig. 2e and b), and (ii) a ∼20° rotation about the MT[111] direction, which is parallel to the needle elongation direction, leads to the COR corresponding to a

PL($\overline{3}$12)n-MT micro-inclusions in nucleation orientation (compare Fig. 2f and c).
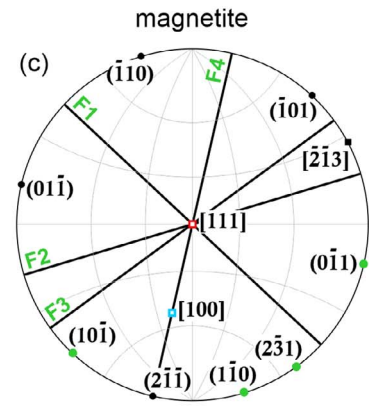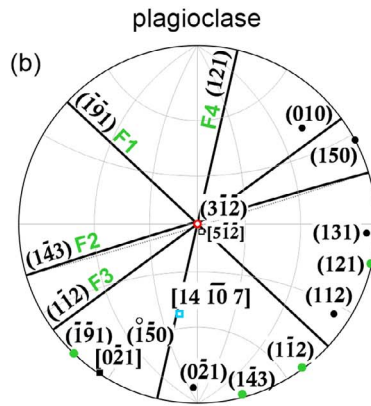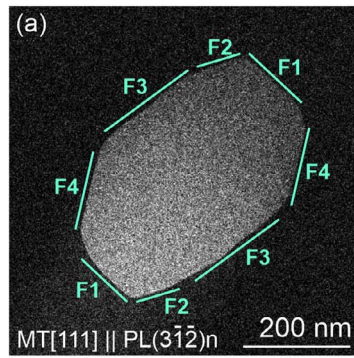
Interface configuration in nucleation orientation

The sides of the hexagonal cross-section of the PL($\overline{3}$12)n-MT inclusion in nucleation orientation are labelled F1 to F4 in Fig. 2a. The traces of these facets are connected by comparatively short segments with outwards convex curvature forming the rounded corners of the hexagonal cross-section. Standard high-resolution bright-field STEM images of the F1, F3 and F4 facets and the transitional area between F1 and F4 are shown in Fig. 3a–e. While the MT($\overline{2}$20), MT($\overline{2}$02) and MT(0$\overline{2}$2) lattice planes are resolved as lattice fringes in Fig. 3a–e, lattice fringes of PL(131), PL(04$\overline{1}$) and PL(1$\overline{1}$2) lattice planes are clearly resolved only in Fig. 3e. This is due to the fact that small rotations and/or tilts exist between the HR-STEM images, as can be inferred from a comparison with the MT{220} lattice fringes. In Fig. 3e, the traces of the MT($\overline{2}$20) lattice planes (solid lines) are 2.5° inclined relative to the yellow dashed line, which represents the orientation of the MT($\overline{2}$20) in Fig. 3d. While the PL(131) lattice planes are edge-on in Fig. 3e, where the direction of the electron beam is parallel to PL[6.5, −1, −3.5] and deviates by 2° from PL($\overline{3}\overline{1}$2)n, they are slightly inclined and are off the diffraction condition, thus only poorly resolved in Fig. 3a–d, where the electron beam is parallel to MT[111] and slightly deviates from PL($\overline{3}$12)n. The configurations of the magnetite–plagioclase interfaces differ between the different facets. Each facet is (sub)parallel to the lattice fringes of at least one of the phases. For example, facet F1 is approximately parallel to MT($\overline{2}$02), facet F3 is approximately parallel to PL(1$\overline{1}$2) and facet F4 is approximately parallel to MT(0$\overline{2}$2). At the transitional area between facets F1 and F4 shown in Fig. 3b, the magnetite–plagioclase interface shows a step-like configuration with the step terraces parallel to facet F1, which is approximately parallel to MT($\overline{2}$02).

Sketches of the geometrical correspondence of the resolved lattice fringes in magnetite and plagioclase across the F1, F3 and F4 facets shown in Fig. 3c–e are presented in Fig. 3g–i. The *d*-spacings of the lattice planes were calculated using the crystallographic data from Wenk *et al.* (1980) for plagioclase and from Fleet (1981) for magnetite, which yield $d_{PL131} = 2.83$ Å, $d_{PL04\overline{1}} = 2.95$ Å, $d_{PL1\overline{1}2} = 2.52$ Å and $d_{MT220} = 2.97$ Å. Along facet F1, the MT(2$\overline{2}$0) lattice planes and the PL(1$\overline{1}$2) lattice planes impinge on the magnetite–plagioclase interface with a frequency of 4:5, while the MT(0$\overline{2}$2) and the PL(04$\overline{1}$) lattice planes impinge with a frequency of 6:3 (Fig. 3h). Furthermore, facet F1 is approximately parallel to MT($\overline{2}$02). Similarly, the MT(0$\overline{2}$2) and the PL(04$\overline{1}$) lattice planes impinge on interface segment F3 with a frequency of 6:7, while the MT($\overline{2}$20) and the PL(131) lattice planes impinge with a frequency of 4:9 (Fig. 3i). Facet F3 is (sub)parallel to MT(2$\overline{3}$1) and PL(1$\overline{1}$2). Apart from this correspondence of lattice planes, additional lattice planes also meet at facet F3 with only small mismatch (indicated with black circles at the interface segment). Along facet F4, the MT($\overline{2}$20) and PL(04$\overline{1}$) lattice planes impinge on the interface with a frequency of 8:9 (Fig. 3g), and the F4 facet is close to parallel to MT(0$\overline{2}$2) and PL(121).

The magnetite–plagioclase interfaces along facets F1, F3 and F4 may thus be considered as commensurate with respect to the MT($\overline{2}$20), MT(0$\overline{2}$2), MT($\overline{2}$02) and PL(1$\overline{1}$2), PL(04$\overline{1}$), PL(131) lattice planes, which are resolved by STEM imaging (Howe *et al.*, 2002). Each facet may contain additional pairs of magnetite and plagioclase lattice planes, which are commensurate along the interfaces, but here we only refer to those lattice planes that are resolved as lattice fringes on the BF STEM images. Despite the lack

MAGNETITE IN NUCLEATION

plagioclase

magnetite

MAGNETITE IN MAIN
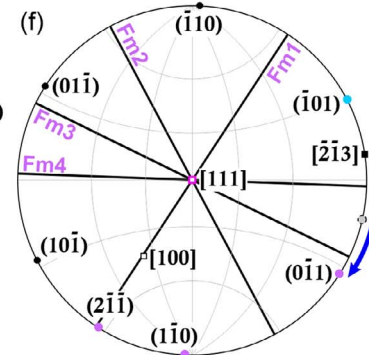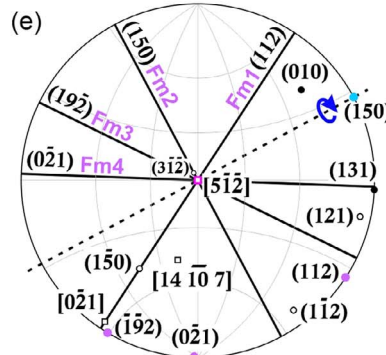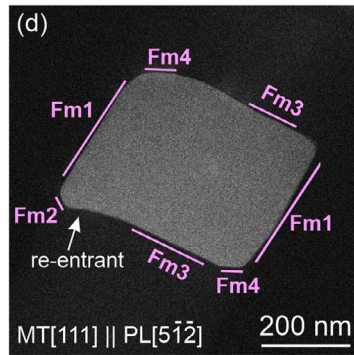
Fig. 2. (a) Standard HAADF STEM image of needle-shaped PL($\overline{3}$12)n-MT micro-inclusions in nucleation orientation viewed in cross-section along MT[111] ‖ PL($3\overline{1}\overline{2}$)n and with interface facets Fi (i = 1–4) indicated. (b,c) Stereographic projections of plagioclase and magnetite showing the COR of PL($\overline{3}$12)n-MT micro-inclusion in nucleation orientation. (d) HAADF cross-section view along MT[111] ‖ PL[$5\overline{1}\overline{2}$] of needle-shaped PL($\overline{3}$12)n-MT micro-inclusions in main orientation. Interface facets are labelled as Fmi (i = 1–4). White arrow points to re-entrant section of the inclusion perimeter. (e,f) Corresponding stereographic projections of plagioclase and magnetite. The orientation of the stereographic projections (b-c) and (e-f) follow reference frame in (a) and (d), respectively. Solid and hollow symbols represent upper and lower hemisphere poles. Crystallographic alignments between magnetite and plagioclase are indicated with the same colour code. Grey circle in (f) represents the MT($0\overline{1}1$) pole in (c). The facets highlighted in (a) and (d) are (sub)parallel to low index lattice planes in plagioclase and in magnetite, respectively. They are indicated by large circles and labelled with Miller indices in (b-c) and (e-f), representing the lattice planes in plagioclase and in magnetite with the same colour codes. The two rotations relating the nucleation and main orientations are indicated with blue arrows in (e) and (f).

Table 2: Conventions for assigning specific Miller indices for the four studied magnetite micro-inclusions and the plagioclase host

| No.	1st alignment	2nd alignment	Category
1	PL($3\overline{1}\overline{2}$) ‖ MT(222)	PL[14,-10,7] ‖ MT[100]	Needle-shaped PL($\overline{3}$12)n-MT inclusion in nucleation orientation
2	PL[$5\overline{1}\overline{2}$] ‖ MT[111]	PL(150) ‖ MT($\overline{1}$01)	Needle-shaped PL($\overline{3}$12)n-MT inclusion in main orientation
3	PL($\overline{3}$12) ‖ MT($22\overline{2}$)	PL(150) ‖ MT($2\overline{2}$0)	Plate-shaped PL($\overline{3}$12)n-MT inclusion in main orientation
4	PL(112) ‖ MT(222)	PL($1\overline{5}$0) ‖ MT($2\overline{2}$0)	Needle-shaped PL(112)n-MT inclusion in main orientation

of a STEM image, facet F2 can be inferred to be close to parallel to MT($2\overline{2}$0) and PL($1\overline{4}$3) by comparing the facet trace with the stereographic projections in Fig. 2b, c.

Interface configuration in main orientation

The cross-section of the inclusion in main orientation (Fig. 2d) has an approximately rectangular shape, which is bounded by straight interface segments referred to as facets Fm1 and Fm3, which are connected by curved segments Fm2 and Fm4. Standard high-resolution BF STEM images of the different interface segments are shown in Fig. 4a-j. In all STEM images, at least one set of MT{220} lattice planes can be resolved as lattice fringes. Due to the beam sensitivity and the complex crystal structure of plagioclase, PL(131) lattice planes are resolved only in Fig. 4c, d, e, g.

The magnetite–plagioclase interface along facet Fm1 on the left side of the rectangle (Fig. 4a) is edge-on, while it appears diffuse and seems to be inclined relative to the incident beam on the right side of the rectangle (Fig. 4d). Along facet Fm1 on the left side of the rectangle, the magnetite–plagioclase interface is nearly parallel to the MT($0\overline{2}2$) and PL(112) lattice fringes. Facets Fm2 are closely parallel to MT($\overline{2}02$) ‖ PL(150) and represent only a small fraction of the magnetite–plagioclase interfaces. Facet Fm3 appears curved in the overview image shown in Fig. 2d, whereas it has relatively sharp straight segments on the nanometre scale as shown in Fig. 4b and diffuse segments as shown in Fig. 4f and h. The straight segments are close to parallel to the MT($\overline{2}11$) ‖ PL($19\overline{2}$) lattice planes (Fig. 4b, g). Fig. 4c shows the transition between Fm3 and Fm1, which appears diffuse and contains two relatively
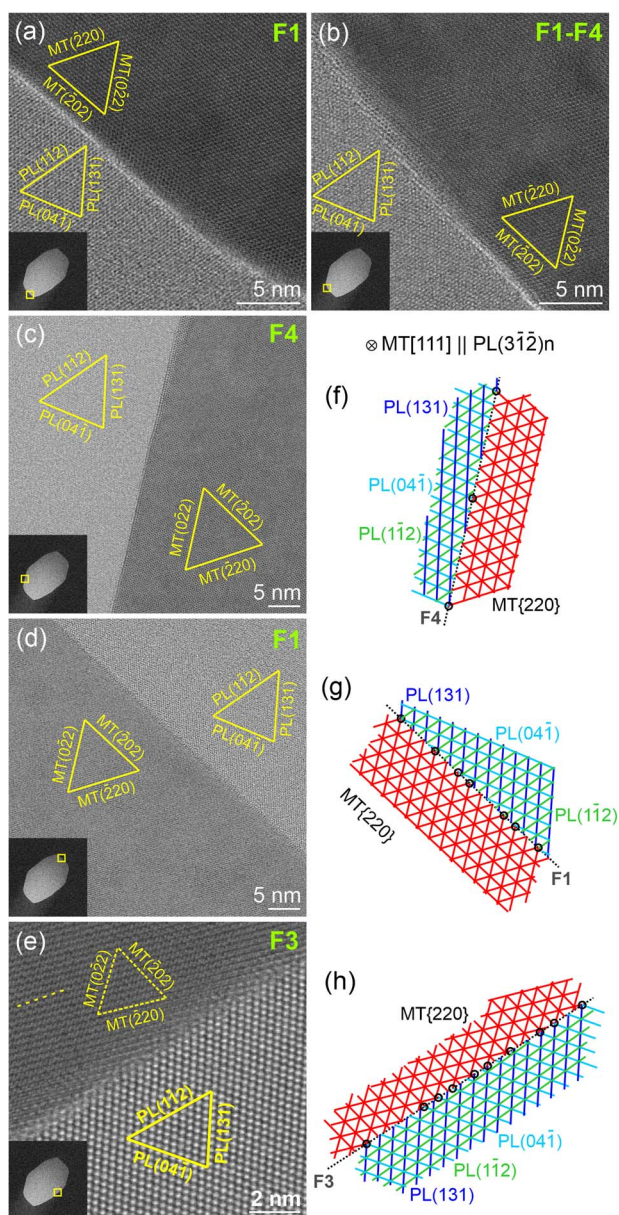
Fig. 3. Standard high-resolution BF STEM images of magnetite–plagioclase interfaces of a PL($\bar{3}$12)n-MT inclusion in nucleation orientation. (a) Facet F1 at the lower part of the hexagonal perimeter, (b) F1-F4 transition, (c) F4, (d) F1 at the upper part of the hexagonal perimeter and (e) F3. An overview of the inclusion cross-section is inserted at the lower-left corner with the locations of the detail images highlighted by yellow squares. Well-resolved magnetite and plagioclase lattice fringes are indicated by solid lines labelled with the respective Miller indices. The yellow dashed line in (e) represent the orientation of the MT($\bar{2}$20) lattice planes in (d). Sketches of the lattice plane correspondence at the magnetite–plagioclase interfaces of facets (g) F4, (h) F1 and (i) F3. Points of (nearly) precise match between magnetite and plagioclase lattice planes are indicated with black circles.

sharp interface segments: one segment is parallel to Fm3, which is parallel to MT($\bar{2}$11), and the second is close to parallel to PL(131). Fig. 4e shows facet Fm4 and the connection to Fm1 at the lower-right corner of the rectangular cross-section. The straight segment of Fm4 is parallel to MT($\bar{2}$20) || PL(02$\bar{1}$). Fig. 4i shows the transition between Fm1 and Fm2, which is curved with changing interface configurations on the nanometer scale. Fig. 4j shows a

sketch of the lattice plane correspondence between magnetite and plagioclase. The contrast seen in the magnetite inclusion in Fig. 4f is ascribed to a defect. The type of the defect can, however, not be determined.

Plate-shaped PL($\bar{3}$12)n-MT micro-inclusion in main orientation

As stated above, needle-shaped PL($\bar{3}$12)n-MT micro-inclusions in main orientation follow the COR, where one of the MT<111> ~ || PL($\bar{3}$12)n, one set of the MT{220} || PL(150) and another set of the MT{220} ~ || PL(112). While the alignment of MT<111> (close) to PL($\bar{3}$12)n gives rise to the preferred elongation direction of the PL($\bar{3}$12)n-MT micro-inclusions, the second alignment of MT{220} || PL(150) may lead to preferred extension in a second direction leading to platy morphology of the micro-inclusion parallel to MT{220} || PL(150). A TEM foil of a plate-shaped PL($\bar{3}$12)n-MT micro-inclusion in main orientation was extracted perpendicular to the MT{220} || PL(150) basal plane of the plate and parallel to the MT[11$\bar{1}$] || PL($\bar{3}$12)n direction (Fig. 5). The incident electron beam is parallel to MT[112] || PL[5$\bar{1}$8]. The MT[11$\bar{1}$] and PL($\bar{3}$12)n directions lie in the plane of the foil, and the magnetite–plagioclase interfaces on either side of the plate, which are parallel to the MT($\bar{2}$20) and PL(150) lattice planes, are edge-on (Fig. 5a). Standard HAADF STEM images of the two plane surfaces are shown in Fig. 5b and c.

The lattice fringes corresponding to the MT(22$\bar{2}$) and MT(2$\bar{2}$0) lattice planes can be well discerned. The inclusion elongation direction is nearly parallel to MT[11$\bar{1}$] as indicated by the white arrow. Detailed iDPC-STEM images of the same interface segments as shown in Fig. 5b and c are presented in Fig. 5d and e. Fig. 5f shows the same interface segment as Fig. 5d after counter clockwise rotation about the viewing direction so that the magnetite–plagioclase interface is horizontal. Lattice fringes in magnetite and in plagioclase are well resolved. Fast Fourier transformation patterns of plagioclase and magnetite obtained from Fig. 5f are shown in supplementary material II Fig. S3. In plagioclase, the lattice fringes corresponding to PL($\bar{1}$31) and PL(22$\bar{1}$) can be seen. Crystal structure models of plagioclase and magnetite oriented corresponding to the crystal orientation in Fig. 5f are shown in Fig. 5g, h. The PL($\bar{1}$31) and PL(22$\bar{1}$) lattice fringes observed in Fig. 5f correspond to cation layers in the crystal structure model. In contrast, no lattice fringes corresponding to the PL($\bar{3}$12) and PL(150) lattice planes can be discerned. The MT(22$\bar{2}$) lattice planes correspond to close-packed oxygen layers in the crystal structure of magnetite (Fig. 5h), and the MT(22$\bar{2}$) || PL($\bar{3}$12) lattice planes are in direct contact across the magnetite–plagioclase interfaces parallel to the inclusion elongation direction. The interface is sharp and fully crystalline, and in the observed domain, there is possibly a step in the interface (Fig. 5f). Nearly identical d-spacing of the corresponding oxygen layers in magnetite and plagioclase ensures semi-coherent alignment of the MT(22$\bar{2}$) and the PL($\bar{3}$12) lattice planes across the magnetite–plagioclase interface bounding the inclusion along the elongation direction. Based on crystallographic data for room temperature and 1 bar pressure reported by Wenk et al. (1980) for plagioclase and by Fleet (1981) for magnetite, the lattice misfit along the MT[11$\bar{1}$] || PL($\bar{3}$12)n direction is $\delta = |d_{PL\bar{3}12} - d_{MT222}|/d_{PL\bar{3}12} = 0.032$, which is likely accommodated by edge dislocation every about 31st MT(22$\bar{2}$) plane at the magnetite–plagioclase interface. This supposition is corroborated by the analysis of Fig. 5f. The interface area in Fig. 5f is rather obscure and potentially occurring edge dislocations and associated half-planes in magnetite cannot be unambiguously identified. Counting the lattice planes further
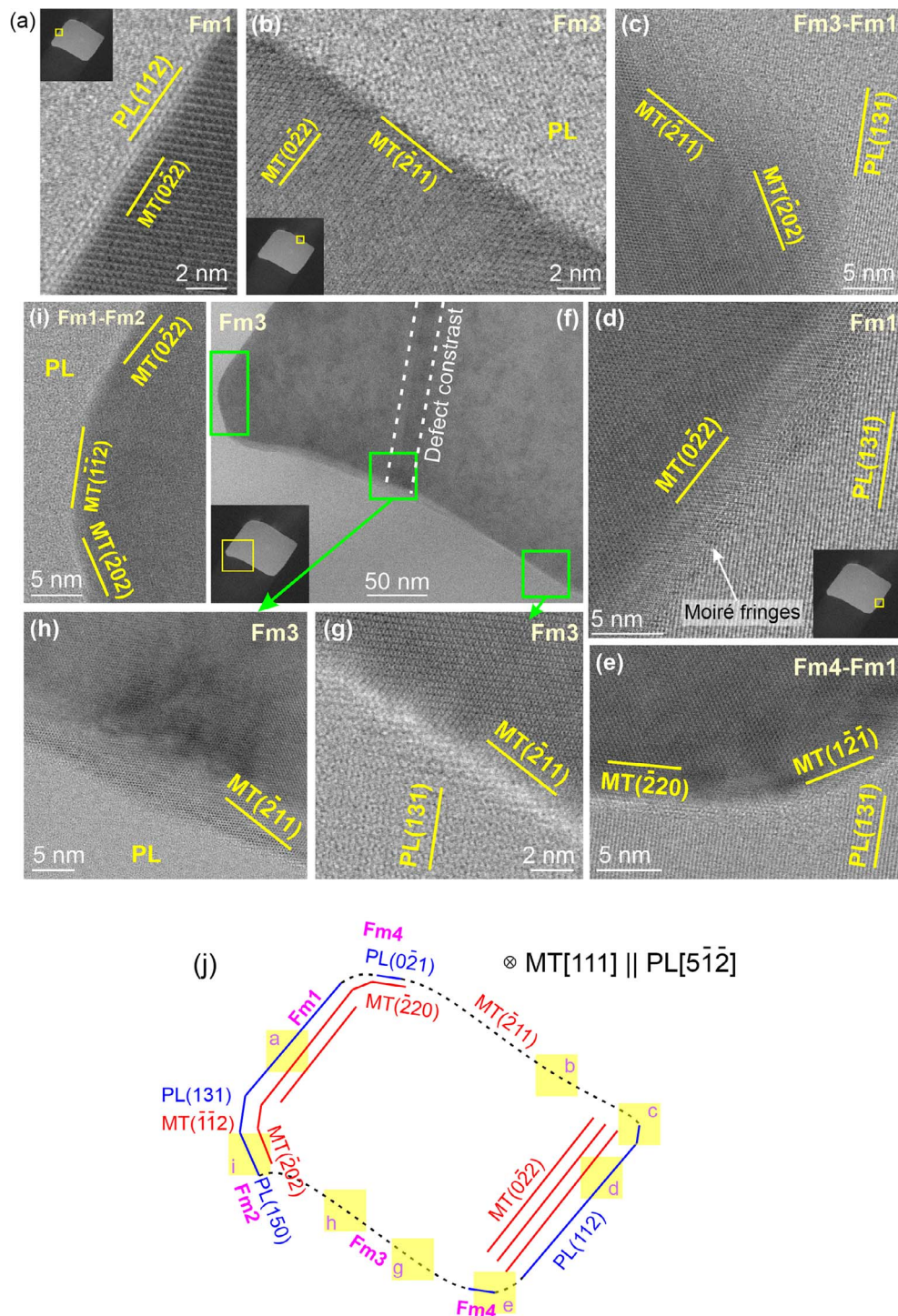
Fig. 4. Standard high-resolution BF STEM images of magnetite–plagioclase interface facets (a) Fm1, (b) Fm3, (c) Fm3-Fm1, (d) Fm1, (e) Fm4-Fm1, (f, g, h) Fm3 and (i) Fm1-Fm2. An overview of the cross-section with the locations of the STEM images is inserted in (a, b, d, f). Lattice planes from both phases and moiré fringes are indicated when observed. (j) Sketch of lattice planes of the two phases alignment at each facet at the magnetite–plagioclase interface. Alphabetically labelled yellow squares represent the acquisition locations of the detailed STEM images. Viewing direction is parallel to MT[111] || PL[$5\bar{1}\bar{2}$] in all images.

away from the interface yields 66 PL($\bar{3}$12) lattice planes and 68 MT(22$\bar{2}$) lattice planes over the viewing area, indicating that two edge-dislocations and associated half-planes of MT(22$\bar{2}$) exist that accommodate the misfit over the interface segment shown in Fig. 5f. The counting of lattice planes was done on an inverse fast Fourier transformation (iFFT) image obtained from Fig. 5f, which is shown in supplementary material II Fig. S3.

Needle-shaped PL(112)n-MT micro-inclusion in main orientation

A needle-shaped PL(112)n-MT micro-inclusion was selected for dedicated atomic scale investigations of the magnetite–plagioclase interface. It is known from prior EBSD analyses that the inclusion is in main orientation according to the classification scheme of Ageeva *et al.* (2020), implying that MT[111] || PL(112)n,
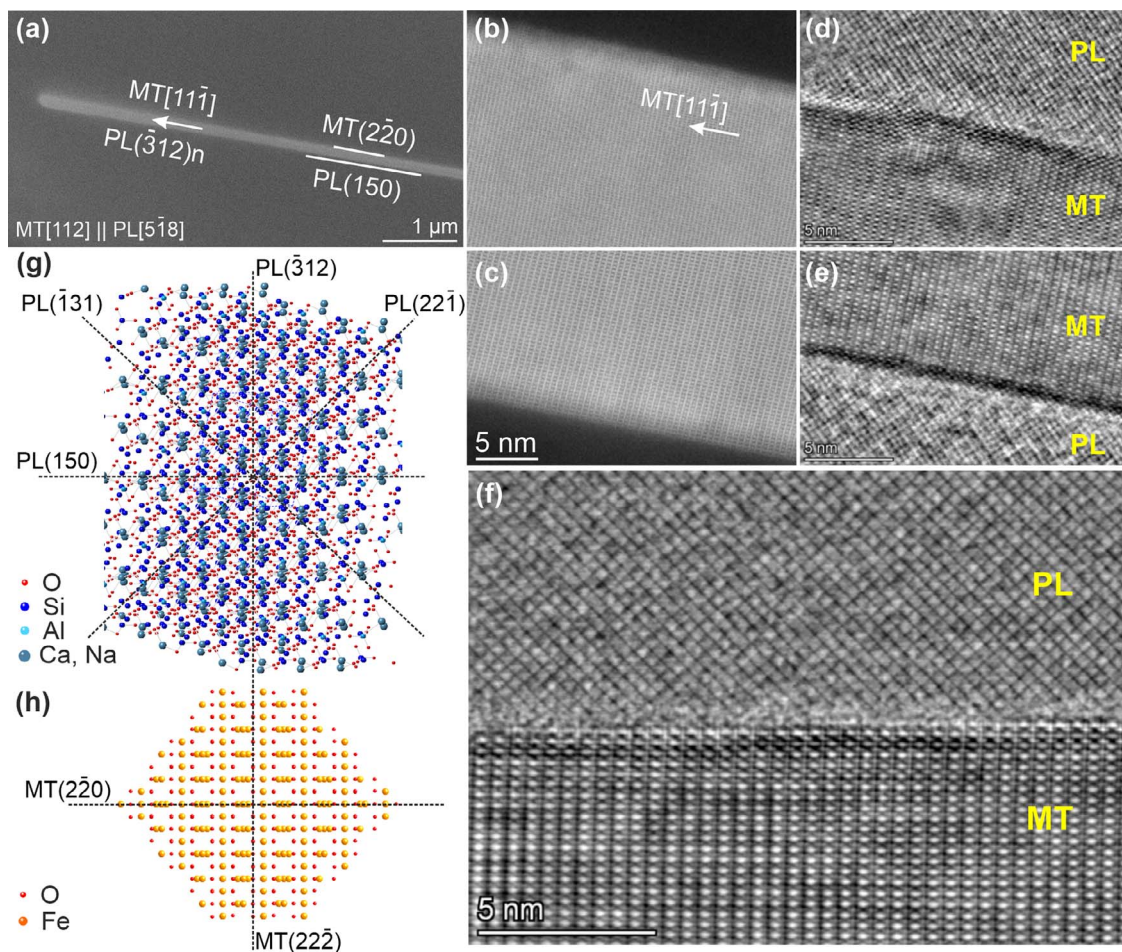
Fig. 5. (a) SE image of a plate-shaped PL($\bar{3}$12)n-MT micro-inclusion after FIB extraction. The inclusion elongation direction (white arrow) lies in the plane of the foil, and the plate surface (white lines) is edge on. (b, c) Standard HAADF STEM imaging of magnetite–plagioclase interface: showing magnetite–plagioclase interfaces corresponding to the MT($2\bar{2}$0) ∥ PL(150) plate surface bounding a plate-shaped PL($\bar{3}$12)n-MT micro-inclusion in main orientation on either side. The intersection of the foil and the plate is parallel to MT[11$\bar{1}$] – white arrow. (d, e) iDPC-STEM images of the magnetite–plagioclase interface from area (b) and (c), respectively. (f) Close-up iDPC-STEM image of the interface segment shows in (d), rotated. MT(22$\bar{2}$) and MT($2\bar{2}$0), PL($\bar{1}$31) and PL(22$\bar{1}$) lattice planes are resolved. (g, h) Crystal structure models of plagioclase and magnetite according to the orientation in f with lattice planes observed in iDPC-STEM images indicated. Viewing direction is parallel to MT[112] ∥ PL[5$\bar{1}$8] in all images. Cations and anions are not shown to scale. In reality, the oxygen atoms are bigger and the cations are smaller. To stress the distribution of the cations and anions, the oxygen atoms are drawn at 1/6 of the real size proportion.

MT($2\bar{2}$0) ∥ PL(1$\bar{5}$0). The inclusion elongation direction is MT[111], which is aligned with the normal direction of the PL(112) plane to within 1.5° as determined by universal stage measurements. Two TEM foils were extracted from this inclusion using SEM-FIB technique, where one foil was cut parallel and the other one was cut perpendicular to the inclusion elongation direction. PL(112)n-MT micro-inclusions are rarely seen in nucleation orientation and therefore results are only shown for a PL(112)n-MT micro-inclusion in main orientation.

Interface configuration along the needle elongation direction

Fig. 6 shows an overview image and details of a PL(112)n-MT micro-inclusion with its elongation direction in the plane of the foil. The viewing direction is parallel to MT[11$\bar{2}$] ∥ PL[51$\bar{3}$] in all images. In the standard HAADF STEM image (Fig. 6a) the inclusion shows wedge shape tapering out to the left. The different grey scales are probably contributed by the non-uniform thickness of the inclusion. In some segments, the magnetite–plagioclase interface appears sharp, in other segments, it is more blurred. At the blurred segments, the interface is accompanied

by a zone of reduced brightness in the magnetite indicating that in these domains the magnetite–plagioclase interface is inclined with respect to the incident electron beam so that the beam penetrates both magnetite and plagioclase in a narrow zone along the magnetite–plagioclase interface. The fact that the zones of reduced brightness only extend along parts of the magnetite–plagioclase interface indicates that the magnetite needle is partly bound by facets, which are inclined relative to the MT[111] direction. Interface segments that appear sharp pertain to facets sharing the MT[111] direction as a common zone axis and also contain the MT[11$\bar{2}$] direction, which is parallel to the viewing direction. The overall 3D geometry of the magnetite needle thus deviates from a plain prism shape. The irregularly shaped domain with different grey shade highlighted by the green rectangle in Fig. 6a was identified as ilmenite based on its comparatively low Fe and high Ti content as seen in the element distribution maps shown in Fig. 6e.

In the iDPC-STEM images shown in Fig. 6b, the lattice fringes of both magnetite and plagioclase are in direct contact along the interface with no amorphous layers or gaps in between. Lattice fringes are resolved in magnetite and in plagioclase. Fast Fourier
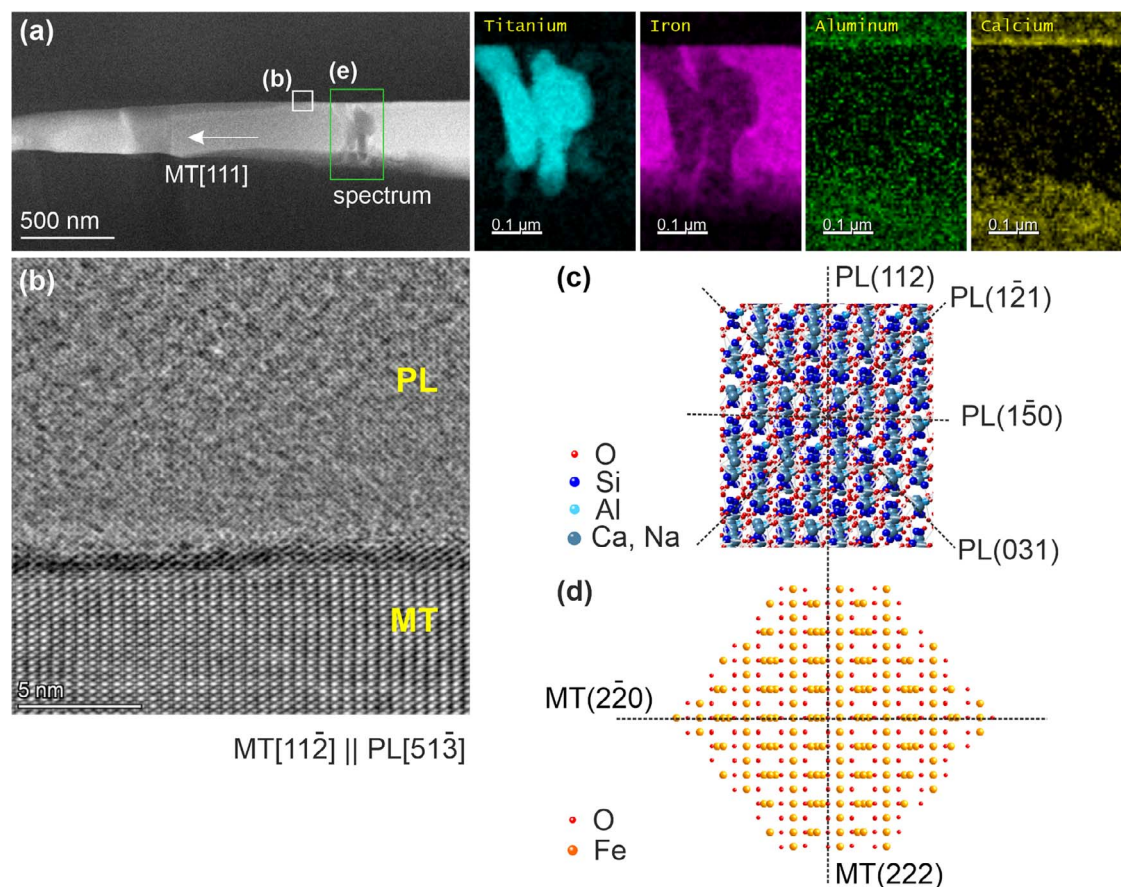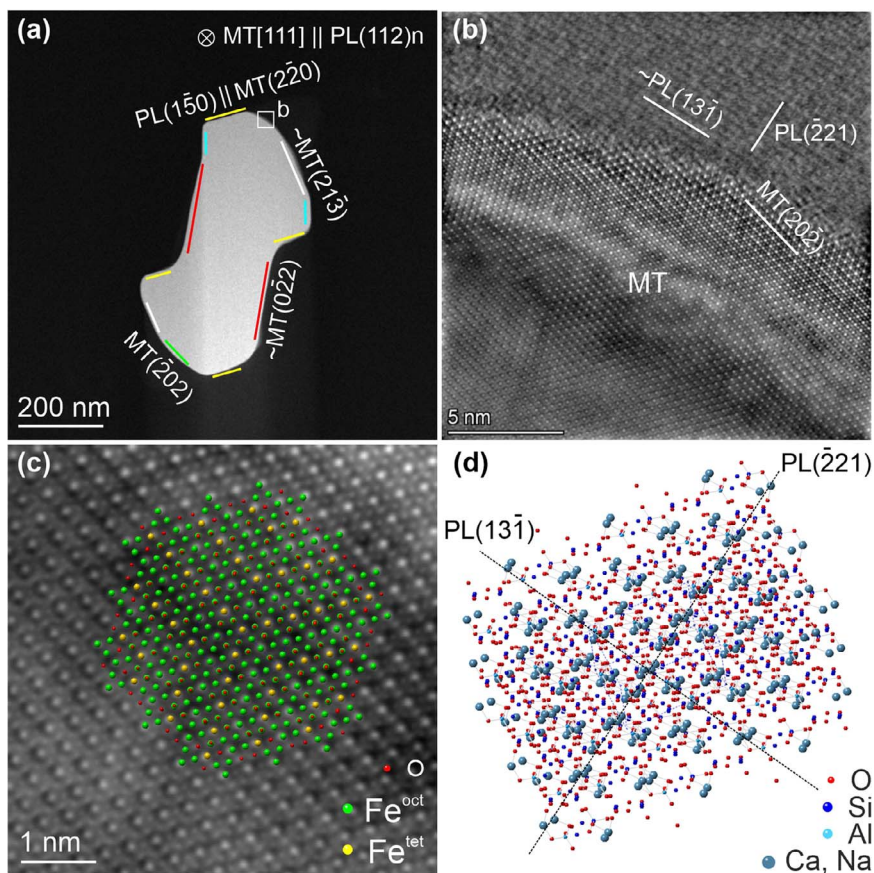
Fig. 6. (a) Standard HAADF STEM image showing an overview of a needle-shaped PL(112)n-MT micro-inclusion in main orientation with its elongation direction oriented horizontally in the plane of the foil. The white rectangle with alphabetic label indicates the scanning area covered by the atomic scale iDPC-STEM image shown in (b). The green rectangle indicates the area covered by the element distribution maps shown in (e). (b) iDPC-STEM image of a magnetite–plagioclase interface segment that is edge on. The MT(222) and MT(2$\bar{2}$0) lattice planes are resolved in magnetite, and the PL(1$\bar{2}$1) and PL(031) lattice planes are resolved in plagioclase. (c, d) Crystal structure models for plagioclase and magnetite according to the orientation in (b) with the lattice planes observed in the iDPC-STEM images indicated: oxygen layers parallel to PL(112) and PL(1$\bar{5}$0), close-packed oxygen plane MT(222) and less densely packed oxygen plane MT(2$\bar{2}$0). (e) STEM-EDS element distribution maps of the area indicated by the green rectangle in (a). Segregation of Ca and Al at the upper magnetite–plagioclase interface. Viewing direction is parallel to MT[11$\bar{2}$] ‖ PL[51$\bar{3}$] in all images. Cations and anions are not shown to scale. In reality, the oxygen atoms are bigger and the cations are smaller. To stress the distribution of the cations and anions, the oxygen atoms are drawn at 1/6 of the real size proportion.

transformation patterns of magnetite and plagioclase obtained from Fig. 6b are shown in supplementary material II Fig. S4. In the iDPC-STEM image the MT(222) lattice fringes are vertical and the MT(2$\bar{2}$0) lattice fringes are horizontal. The lattice fringes observed in plagioclase are PL(1$\bar{2}$1) and PL(031), and the fringes of the PL(112) planes can be seen only vaguely. The crystal structure models in Fig. 6c–d are oriented according to the observed COR and show that in plagioclase and in magnetite cation clusters are responsible for the detectable lattice fringes under iDPC-STEM imaging, while the MT(222) lattice planes correspond to close-packed oxygen layers in magnetite. Rugged planes parallel to PL(112) dominated by oxygen alternating with layers dominated by cations are visible in the crystal structure model of plagioclase, when viewed along the PL[51$\bar{3}$] direction. The d-spacings of MT(222) and PL(112) are very similar, and the two lattice planes are aligned nearly parallel across the magnetite–plagioclase interface. A slight misalignment of about 1° between the two lattice planes is noticeable in Fig. 6b, suggesting a small tilt component may exist across the interface. Based on the lattice constants reported by Fleet (1981) and Wenk *et al.* (1980), the lattice misfit between MT(222) and PL(112) is calculated as $\delta = |d_{PL112} - d_{MT222}| / d_{PL112} = 0.016$. Thus, edge dislocations are expected to be present at every

~63rd MT(222) plane at the magnetite–plagioclase interface to accommodate the 1.6% lattice misfit. The presence of a misfit dislocation can indeed be inferred from an analysis of the iFFT image obtained from Fig. 6b, where 69 PL(112) lattice planes on one side of the magnetite–plagioclase interface correspond to 70 MT(222) lattice planes on the other side of the interface, indicating that one MT(222) half-plane exists at the magnetite–plagioclase interface in this area. The iFFT results are included in supplementary material II Fig. S4. The interface segment covered by scan area b in Fig. 6 is perpendicular to the plane of the foil and is thus viewed edge on. The interface is parallel to the MT(2$\bar{2}$0) and the PL(1$\bar{5}$0) lattice planes. It is seen in the crystal structure models that densely packed oxygen planes extend parallel to the MT(2$\bar{2}$0) lattice plane and less well defined but still well-discernible oxygen layers extend parallel to the PL(1$\bar{5}$0) lattice planes in plagioclase. Both these oxygen layers are aligned parallel to the magnetite–plagioclase interface. Locally elevated Ca and Al concentrations are observed within a few nm wide zone in the plagioclase along the upper magnetite–plagioclase interface in the area labelled e, indicating segregation of these elements at the interface (Fig. 6e). The Ca and Al enrichment at the magnetite–plagioclase interface implies an elevated anorthite

Fig. 7. (a) Standard HAADF STEM overview image showing the cross-section of the PL(112)n-MT micro-inclusion shown in Fig. 6, viewing direction is MT[111] ∥ PL(112)n. The traces of specific lattice planes in magnetite and in plagioclase are indicated with coloured lines. The white rectangle corresponds to the scan area covered by the iDPC-STEM image in (b). (b) iDPC-STEM image of a curved magnetite–plagioclase interface segment with three sets of lattice planes sharing the viewing direction as their common zone axis indicated. (c) Crystal structure model of magnetite overlain on a close up of the iDPC-STEM image shown in (b). Fe^{tet} and Fe^{oct} represent tetrahedrally and octahedrally coordinated Fe atoms, respectively. (d) Crystal structure model of plagioclase oriented according to the plagioclase orientation in (b). Discernible lattice fringes in (b) are indicated and correspond to distributed cation clusters. Cations and anions are not shown to scale. In reality, the oxygen atoms are bigger and the cations are smaller. To stress the distribution of the cations and anions, the oxygen atoms are drawn at 1/6 of the real size proportion.

content adjacent to the magnetite micro-inclusions as compared to the plagioclase matrix. The observed segregation was likely acquired in the course of dissolution and recrystallisation of the plagioclase during magnetite growth. The local enrichment is less pronounced along the lower magnetite–plagioclase interface, which is probably due to the fact that the upper interface is edge-on, while the lower interface is inclined relative to the incident beam. The inclination of the lower interface is also manifest from the gradually decreasing intensities of the Fe and Ti signals along a transect from the magnetite to the plagioclase (Fig. 6e).

Interface configuration of the needle cross-section

In Fig. 7a, a standard HAADF image of a cross-section of the PL(112)n-MT micro-inclusion shown in Fig. 6 is presented. The viewing direction is parallel to the inclusion elongation direction, and thus coincides with MT[111] ∥ PL(112)n. The variation of the greyscale in the magnetite domain is due to curtaining effect induced during FIB preparation. STEM-EDS element distribution maps of the sample are shown in supplementary material II Fig. S5. The inclusion cross-section has a nearly centro-symmetrical shape and is bounded by a number of differently oriented straight or slightly curved interface segments. Interestingly, the individual interface segments are connected by both outwards convex and outwards concave segments. Specific lattice planes in magnetite

and plagioclase that are close to parallel to different interface segments are indicated by coloured lines in Fig. 7a. The facet orientations are derived from the iDPC-STEM image in Fig. 7b. Most facets appear in pairs bounding the inclusion on opposing sides. The facet pair highlighted with the straight yellow lines in Fig. 7a is special in that it is parallel to both MT(2$\bar{2}$0) and PL(1$\bar{5}$0). This also corresponds to the interface trace presented in Fig. 6b. The other interface segments are close to parallel to low-index lattice planes in magnetite, the indices are indicated in Fig. 7a, but no parallel alignment to low-index lattice planes in plagioclase can be identified. Fig. 7b shows an iDPC-STEM image of the magnetite–plagioclase interface at a segment with outwards convex curvature. In magnetite, individual atomic columns are resolved and the lattice fringes corresponding to the MT(2$\bar{2}$0) can be inferred (Fig. 7c). In plagioclase, the lattice fringes of the PL(13$\bar{1}$) and PL($\bar{2}$21) lattice planes can be discerned even though they are slightly off zone axis. As can be seen in the crystal structure model shown in Fig. 7d, they correspond to linearly distributed clusters of cations in the plagioclase crystal structure.

DISCUSSION
Plane-normal magnetite micro-inclusions

From petrographic evidence abundant needle-shaped PL(112)n-MT, PL($\bar{3}$12)n-MT, PL(100)n-MT and rare PL(150)n-MT

micro-inclusions as well as abundant PL[001] inclusions and a few plate-shaped magnetite inclusions were identified in the investigated plagioclase grain (Fig. 1). Whereas the first four inclusion types pertain to the plane-normal inclusions according to Ageeva et al. (2020), the PL[001] inclusions pertain to a fundamentally different inclusion type. Bian et al. (2021) inferred that the magnetite micro-inclusions of the plane-normal type represent the first generation of plagioclase-hosted oriented magnetite micro-inclusions that formed by precipitation from Fe-bearing plagioclase in the course of a solid-state reaction or a sequence of solid-state reactions. In contrast, even though in the investigated plagioclase domain, the PL[001] inclusions occur together with the plane-normal inclusions and may be coeval, the PL[001] inclusions are generally ascribed to later hydrothermal processing and recrystallisation (Bian et al., 2021; Ageeva et al., 2022). The following discussion is restricted to the plane-normal type inclusions.

The elongated shape of plane-normal type magnetite micro-inclusions was ascribed to the good match of lattice planes corresponding to oxygen layers in both magnetite and plagioclase across the interfaces that contain the needle elongation direction (Ageeva et al., 2020). The associated CORs were ascribed either to configurations that facilitate nucleation (Ageeva et al., 2020), fast growth (Wenk et al., 2011), or to configurations that minimise interfacial energy (Ageeva et al., 2020), and elastic strain energy (Wenk et al., 2011). The CORs corresponding to the nucleation orientation have been related to the favourable orientation of FeO_6 octahedra, which are important building units of magnetite, in channels running parallel to the PL[001] direction in the crystal structure of plagioclase (Wenk et al., 2011; Ageeva et al., 2020). Accommodation of the FeO_6 octahedra in the channels of the plagioclase crystal structure most likely decreases the nucleation barrier for magnetite (Wenk et al., 2011). The nucleation barrier is mainly due to the generation of interfaces between the nucleus and the host (Sutton & Balluffi, 1995; Christian, 2002). Therefore, the nuclei tend to form coherent interfaces. Generally, a certain lattice misfit exists between the precipitate and the host, and such coherency will become exceedingly difficult to maintain, when the precipitate grows. This also applies to magnetite plagioclase pairs and, thus, the CORs between magnetite precipitates and the plagioclase host may change during precipitate growth. In the following, the preference of elongation directions, the associated CORs and interface configurations are discussed for the plane-normal type magnetite micro-inclusions in plagioclase.

Nucleation orientation and main orientation

Among the plane normal magnetite micro-inclusions, the PL($\bar{3}$12)-n MT inclusions are special in that they show approximately equal abundances of the orientation variants corresponding to nucleation and main orientation. Typically, as compared to needle-shaped plane normal magnetite micro-inclusions in main orientation, needle-shaped plane normal magnetite micro-inclusions in nucleation orientation show several features that are considered as primary. For example, their elongation direction is usually strictly aligned with the respective PL(hkl) plane-normal direction (Fig. 2b, c). In addition, the inclusions in nucleation orientation typically show regularly shaped faceted cross-sections, which are outwards convex all along the cross-section perimeter (Fig. 2a). The interface facet orientations are mostly related to MT{220} lattice planes, whereas plagioclase lattice planes appear to influence the selection of interface facets less strongly (Fig. 3a, c, d). The relation to the crystal lattice of the

plagioclase host is reflected by the commensurate impingement of plagioclase and magnetite lattice planes along the magnetite–plagioclase interfaces (Fig. 3g, h, i).

In contrast, the elongation direction of magnetite micro-inclusions in main orientation typically deviates by a few degrees from the respective PL(hkl) plane-normal direction (Fig. 2e, f). In addition, magnetite micro-inclusions in main orientation usually show more complex shapes in cross-section with only a few faceted interface segments connected by curved interface segments, which may be outwards concave leading to locally re-entrant sections of the magnetite–plagioclase interface (Fig. 2d). Moreover, the faceted interface segments typically are aligned parallel to low index lattice planes of both magnetite and plagioclase. For example, the PL($\bar{3}$12)-n MT inclusion in main orientation shows nearly perfect parallel alignment of the prominent interface facet Fm1 with MT(0$\bar{2}\bar{2}$) ‖ PL(112) and of the less common facet Fm2 with MT($\bar{2}$02) ‖ PL(150). Based on the plagioclase crystal structure of Wenk et al. (1980), the angle between PL($\bar{3}$12) and PL(150) is 91.23°, and between PL($\bar{3}$12) and PL(112), it is 85.06°. The strong parallel alignments of MT(0$\bar{2}\bar{2}$) with PL(112) and of MT($\bar{2}$02) with PL(150), while keeping the tilt of MT(111) relative to PL($\bar{3}$12) at a minimum, can thus well explain the about 5° deviation of the inclusion elongation direction from the PL($\bar{3}$12)-n direction (Fig. 2e, f). Also, the COR of the plate-shaped PL($\bar{3}$12)-n MT inclusion corresponds to the main orientation. The basal plane of the plate is parallel to the MT(2$\bar{2}$0) ‖ PL(150) lattice planes, which correspond to oxygen layers in both phases. Finally, for the needle-shaped PL(112)n magnetite micro-inclusion, the inclusion elongation direction is aligned parallel to the PL(112)n direction to within about 1.5°, and the most prominent interface segment is aligned parallel with MT(2$\bar{2}$0) ‖ PL(1$\bar{5}$0). The angle between PL(112) and PL(1$\bar{5}$0) is 91.12°. Strictly parallel alignment of MT(2$\bar{2}$0) parallel to PL(1$\bar{5}$0), while keeping the tilt of MT(111) relative to PL(112) at a minimum, thus leads to a 1.12° deviation of the needle elongation direction from the PL(112)-n direction, which is well compatible with our observations. The observed CORs and SORs ensure continuity of the oxygen sub-lattices of magnetite and plagioclase across their interfaces. This is probably due to the fact that oxygen is rather immobile and the inclusion–host orientation relationships as well as the interface orientations organise themselves into configurations that minimise the extent of the re-arrangement of oxygen during growth of magnetite from plagioclase (Hwang et al., 2010; Tan et al., 2022).

Inclusion elongation direction

The elongation direction of needle- and lath-shaped precipitates is usually parallel to the interfaces with the best lattice match between the precipitate and the host crystal (Dahmen et al., 1984; Zhang, 2020). This rationale applies to all plagioclase hosted plane-normal type magnetite micro-inclusions. All these inclusions are elongated parallel to one of the MT<111> directions, which, in turn, is aligned (sub)parallel to the normal direction of one of seven specific plagioclase lattice planes, including PL(112), PL($\bar{3}$12), PL(150), PL(1$\bar{5}$0), PL(100), PL($\bar{3}$1̄2) and PL(1$\bar{1}$2). In the crystal structure of plagioclase, an alternation of oxygen-rich and cation-rich layers exists parallel to these specific lattice planes, and in the crystal structure of magnetite, densely packed oxygen layers are present parallel to MT{222}. The d-spacing of MT{222} is nearly identical to the d-spacing of the specific lattice planes in plagioclase. Thus, the densely packed oxygen layers in magnetite and the oxygen rich layers in plagioclase match very well. In particular, they are nearly coherent across the interface containing the

Table 3: *d*-spacing of specific plagioclase lattice planes relevant for plane-normal inclusions and misfit δ calculated based on $d_{MT222} = 2.42$ Å (Fleet, 1981); crystallographic data for plagioclase were taken from Wenk *et al.* (1980)

PL(*hkl*)	*d*-spacing / Å	Oxygen layers in plagioclase	N	$|\delta|$
112	2.46	Dense	1	0.016
$\overline{3}12$	2.50	Dense	1	0.032
150	2.40	Dense	1	0.012
$1\overline{5}0$	2.45	Dense	1	0.012
100	7.34	-	3	0.009
$\overline{3}\overline{1}2$	2.52	-	1	0.039
$1\overline{1}2$	2.53	-	1	0.042

corresponding MT<111> direction and the plane normal to either one of the PL(112), PL($\overline{3}12$), PL(150), PL($1\overline{5}0$), PL(100), PL($\overline{3}\overline{1}2$) and PL($1\overline{1}2$) lattice planes as the common zone axis. Even though this ensures good lattice match at the interface in only one dimension (Howe *et al.*, 2002), it is regarded as the crystallographic base for the preferred elongation directions of the different plane normal inclusion types (Ageeva *et al.*, 2020). In detail, some lattice mismatch occurs even along the direction of good match, which can be accommodated either by elastic strain or by the introduction of misfit dislocations. Along the direction of good match, the following condition must hold (Howe, 1997):

$$\left| d_{PLhkl} \right| = N \times \mid d_{MT222} \mid \times (1 + \delta),$$

where N is a positive integer, d_{PLhkl} is the *d*-spacing of the PL(*hkl*) lattice plane corresponding to oxygen-rich layers in the crystal structure of plagioclase, d_{MT222} is the *d*-spacing of MT(222) and δ is the lattice misfit. If $\delta = 0$, every MT(222) lattice plane will coincide precisely with every N'th PL(*hkl*) lattice plane. The smaller N, the higher the fraction of lattice planes that are coherent across the interface. The preferred elongation direction with respect to the plagioclase lattice planes and the corresponding N and δ values are listed in Table 3. The lattice constants of magnetite and plagioclase were taken from Fleet (1981) and Wenk *et al.* (1980), respectively. According to Weatherly & Nicholson (1968), misfit values of $|\delta| \leq 0.05$ allow formation of partially coherent precipitates. All seven orientation classes of the plane-normal needles fall into this range.

Effect of temperature

The plane-normal type magnetite micro-inclusions probably formed at high temperature above ~600°C (Bian *et al.*, 2021), and thermal expansion needs to be taken into account when testing for geometrical match between the lattices of magnetite and plagioclase. The lattice parameters of magnetite are available from neutron diffraction at temperatures from 25°C to 800°C (Levy *et al.*, 2012). The lattice parameters of plagioclase with compositions Ab_{100}, $An_{27}Ab_{73}$, $An_{35}Ab_{65}$, $An_{46}Ab_{54}$, $An_{60}Ab_{40}$, $An_{78}Ab_{22}$, $An_{89}Ab_{11}$, $An_{96}Ab_4$ and An_{100} are available from high resolution synchrotron X-ray powder diffraction for temperatures ranging from 25°C to 620°C, where Ab and An are the mole fractions of the albite ($NaAlSi_3O_8$) and anorthite ($CaAl_2Si_2O_8$) components (Tribaudino *et al.*, 2010). The thermal expansion of plagioclase shows substantial anisotropy, where the direction with maximum thermal expansion accounts for over 70% of the total volume change, and it is close to parallel to the plane

normal to the PL(100) lattice plane. This is close to the direction of the characteristic crankshaft-like chains of SiO_4 and AlO_4 tetrahedra in the crystal structure of plagioclase (Brown *et al.*, 1984; Tribaudino *et al.*, 2010). In Fig. 8 the *d*-spacing of the MT(222) lattice planes is compared with the *d*-spacing of plagioclase $An_{60}Ab_{40}$ lattice planes that are parallel to the basal planes of the different plane normal inclusion types. It is seen that the temperature dependence is highest for d_{MT222}. At temperatures above about 600°C, the *d*-spacing of PL($1\overline{5}0$), PL(300) and PL(112) are closest to d_{MT222}, the *d*-spacing of PL($\overline{3}12$) is substantially higher and the *d*-spacing of PL(150) is substantially lower. The *d*-spacing difference between MT(222) and the different PL lattice planes does not appear to control the relative abundances of the different inclusion orientation classes. For example, although the *d*-spacing of PL(112) is never the closest to the *d*-spacing of MT(222), the PL(112)n inclusions are the most frequently observed inclusion type. This is why we infer that the lattice misfit across magnetite–plagioclase interfaces parallel to the needle elongation direction is important for defining the SOR, but it does not explain the relative abundances of the needles pertaining to the different orientation classes. The relatively high abundance of PL(112)n magnetite micro-inclusions may rather be due to the fact that plagioclase is relatively soft parallel to the PL(112)n direction as may be inferred from its relatively high coefficient of thermal expansion in this direction.

Selection of interface facets

Generally, it may be hypothesised that in microstructural equilibrium the interfaces bounding a crystalline precipitate in a host crystal will assume a configuration that minimises the free energy of the precipitate–host system (Sutton & Balluffi, 1995; Howe, 1997). The existence of faceted magnetite–plagioclase interfaces suggests that interface orientations are controlled by crystal structure. From our observations, we infer that in detail the selection of specific interface facets may be guided by different factors. For example, the interface segments F1 and F3 of the needle-shaped PL($\overline{3}12$)n-MT inclusion in nucleation orientation shown in Fig. 3 were probably selected, because of the lattice match with lattice planes of magnetite and plagioclase meeting at the interface in a commensurate manner. In contrast, interface segment F4 was probably selected, because of its parallel alignment with low-index lattice planes of both magnetite and plagioclase.

Apart from minimising interfacial energy in microstructural equilibrium, the shape of a precipitate and its interface configuration may also be controlled by kinetic factors. For example, the interface configuration may be selected that minimises the nucleation barrier and/or allows for fastest growth. Some heterogeneous phase transformations follow a path that minimises atomic movements (Christian, 2002). The COR of the PL(112)n-MT micro-inclusion in main orientation can be expressed as the parallel alignment of the PL(112) and the MT(222) lattice planes combined with a directional match within these planes, namely the parallel alignment of the PL($\overline{1}\overline{1}1$) and MT($\overline{1}01$) lattice directions, which are close-packed directions in the crystal structure of magnetite. According to the lattice parameters given by Wenk *et al.* (1980) for plagioclase and by Fleet (1981) for magnetite, the spacing between two lattice points along PL($\overline{1}\overline{1}1$) is 1.8528 nm, and between two lattice points along MT($\overline{1}01$) is 0.5936 nm. Therefore, every third lattice point in magnetite along MT($\overline{1}01$) has a close match with a lattice point in plagioclase along PL($\overline{1}\overline{1}1$). The parallel alignment of two densely packed oxygen layers and of two directions within the oxygen layers minimises the extent of rearrangement of oxygen
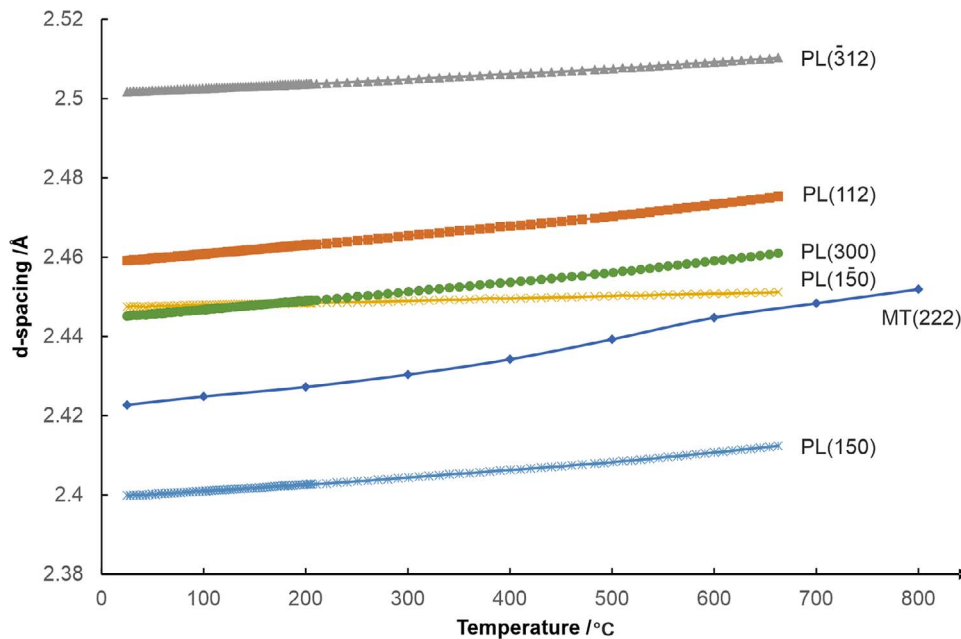
Fig. 8. *d*-spacings of MT(222) and selected plagioclase lattice planes as a function of temperature; crystallographic data were taken from Tribaudino *et al.* (2010) for $An_{60}Ab_{40}$ (labradorite) and from Levy *et al.* (2012) for magnetite.
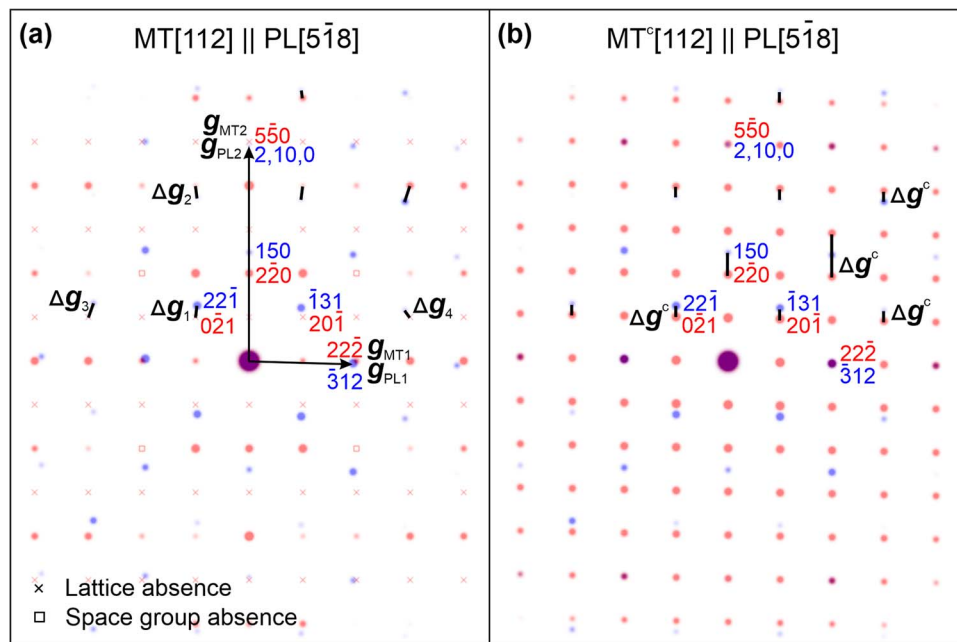
Fig. 9. (a) Diffraction patterns of magnetite (red spots) and plagioclase (blue spots) superimposed according to the COR in Fig. 5f. Viewing direction is MT[112] ‖ PL[5$\bar{1}$8]. Nearly coincident **g** vectors from magnetite and plagioclase are indicated by black arrows emanating from the origin. Representative $\Delta\boldsymbol{g}_i$ (i = 1 − 4) vectors with different directions and lengths are marked with black lines connecting plagioclase and magnetite diffraction spots. (b) Superposition of diffraction patterns of constrained magnetite (red spots) and plagioclase (blue spots) according to the COR in Fig. 5f. The $\Delta\boldsymbol{g}_i$ vectors now become $\Delta\boldsymbol{g}^c$ vectors. All are vertical and parallel to each other (black lines). The trace of the plate surface is perpendicular to all the $\Delta\boldsymbol{g}^c$s and is thus horizontal. Viewing direction is MT^c[112] ‖ PL[5$\bar{1}$8]. Low index lattice planes of magnetite (red) and plagioclase (blue) are indicated next to the corresponding diffraction spots. Symbols × and □ represent the forbidden diffraction spots, which are caused by lattice and space group, respectively.

atoms during the transformation of plagioclase to magnetite, which probably eases nucleation and growth of magnetite in plagioclase (Dahmen, 1982; Wayman, 1994). The PL(112)n-MT micro-inclusion may thus nucleate directly in main orientation. The slight lattice mismatch along MT[$\bar{1}$01] and PL[$\bar{1}\bar{1}$1] may lead to the small deviation from parallel alignment between PL(112) and MT(222), which is usually less than 2° (Zhang, 2020).

Crystal structure control on plate-shaped magnetite micro-inclusion

In Fig. 9a simulated diffraction patterns of magnetite (red spots) and plagioclase (blue spots) viewed along MT[112] ‖ PL[5$\bar{1}$8] are superimposed according to the COR of the plate-shaped PL($\bar{3}$12)n-MT micro-inclusion shown in Fig. 5f. In reciprocal space, a set of (*hkl*) lattice planes is represented by the so-called $\boldsymbol{g}_{hkl}$ vector,

a vector emanating from the origin and pointing to the corresponding hkl diffraction spot. The $\boldsymbol{g}_{hkl}$ vector is perpendicular to the respective set of (hkl) lattice planes in real space, and its length is $1/d$, where d is the d-spacing of the (hkl) lattice planes. A vector $\Delta\boldsymbol{g}$ can be defined as the difference vector between a $\boldsymbol{g}_{hkl}$ vector of one phase and a $\boldsymbol{g}_{hkl}$ vector of the other phase (Zhang & Purdy, 1993). Some $\Delta\boldsymbol{g}$ vectors connecting pairs of closely spaced diffraction spots, where one pertains to magnetite and the other one pertains to plagioclase, are shown as black lines in Fig. 9a. It can be demonstrated by geometrical construction that the two sets of lattice planes, the diffraction spots of which are related by the vector $\Delta\boldsymbol{g}$, are perfectly coherent across a planar interface between the two phases that is perpendicular to the $\Delta\boldsymbol{g}$ vector. If in the superposed diffraction patterns of two phases, two or more non-equivalent $\Delta\boldsymbol{g}$ vectors are parallel to each other, all lattice planes containing the viewing direction as the common zone axis are coherent across a planar interface that is perpendicular to the respective $\Delta\boldsymbol{g}$ vector. The $\Delta\boldsymbol{g}$ vectors connecting closely spaced diffraction spots of magnetite and plagioclase shown in Fig. 9a have all different directions, so that an exact phase boundary configuration cannot be identified. The situation can, however, be changed by applying a strain to either one or both of the lattices. In Fig. 9a two pairs of nearly coinciding $\boldsymbol{g}$ vectors one pertaining to magnetite and the other pertaining to plagioclase have been identified. One pair is represented by $g_{PL1} = \mathrm{PL}(\bar{3}12)$ and $g_{MT1} = \mathrm{MT}(22\bar{2})$ and the other by $g_{PL2} = \mathrm{PL}\,(2,10,0)$ and $g_{MT2} = \mathrm{MT}(5\bar{5}0)$. The two pairs of nearly coinciding $\boldsymbol{g}$ vectors can be made perfectly coincident by applying a constraint on one or both of the two lattices. The resulting relationship between the two lattices is referred to as the *constrained coincidence site lattice* (CCSL) (Ye & Zhang, 2002). The choice of which diffraction spots are made coincident by application of a constraint is arbitrary, but usually two criteria are employed to guide the selection: (i) the diffraction spots that are closest in reciprocal space should be selected to minimise the necessary strain; (ii) the unit cell of the resulting CCSL should be as small as possible, so that the density of CCSL points in direct space is high (Zhang et al., 2000; Ye & Zhang, 2002; Shi et al., 2013). The aforementioned two pairs of $\boldsymbol{g}$ vectors meet both criteria. However, they define the correspondence between the lattices of magnetite and plagioclase only in the plane perpendicular to the viewing direction. An additional constraint is needed in the third dimension to fully fix the correspondence between the two lattices. We chose the viewing direction $\mathrm{MT}[112]$ $\|$ $\mathrm{PL}[5\bar{1}8]$, where the length of vector $\mathrm{MT}[112]$ is 2.0561 Å and the length of vector $\mathrm{PL}[5\bar{1}8]$ is 5.5870 Å. To keep the constraint in the third dimension small, we chose $\mathrm{PL}[5\bar{1}8]/5$ and $\mathrm{MT}[112]/2$ as the reference vectors. The two pairs of selected diffraction spots and the selected lattice vectors in viewing direction are made coincident by applying a constraint on the lattice of magnetite. The procedure is described in the appendix. The resultant lattice parameters of the constrained magnetite MT^c are given in Table 4.

In Fig. 9b the superposition of the simulated diffraction patterns of constrained magnetite (red spots) and of plagioclase (blue spots) are shown for the same orientation relation and viewing direction as in Fig. 9a. Now the pairs of originally nearly coinciding $\boldsymbol{g}$ vectors, namely $g_{PL1} = \mathrm{PL}(\bar{3}12) - g^c_{MT1} = \mathrm{MT}^c(22\bar{2})$ and $g_{PL2} = \mathrm{PL}\,(2,10,0) - g^c_{MT2} = \mathrm{MT}^c(5\bar{5}0)$, where superscript 'c' refers to constrained magnetite, have become coincident.

The $\Delta\boldsymbol{g}$ vectors, $\Delta\boldsymbol{g}_i = \boldsymbol{g}_{MT} - \boldsymbol{g}_{PL}$ $(i = 1-4)$, which all have different directions in Fig. 9a have become the $\Delta\boldsymbol{g}^c = \boldsymbol{g}^c_{MT} - \boldsymbol{g}_{PL}$ vectors in Fig. 9b, which are all parallel to each other and have orientations $\Delta\boldsymbol{g}^c \perp \mathrm{MT}(1\bar{1}0)$ and $\Delta\boldsymbol{g}^c \perp \mathrm{PL}(150)$. Thus, in the

Table 4: Lattice constants of magnetite (MT) (Fleet, 1981), of constrained magnetite (MT^c) when magnetite–plagioclase interface of $\mathrm{PL}(\bar{3}12)$n-MT plate inclusion is coherent

Phase	a / Å	b / Å	c / Å	α / °	β / °	γ / °
MT	8.3970	8.3970	8.3970	90	90	90
MT^c	8.5730	8.4216	8.3785	91.4792	92.4834	89.6406

constrained situation, all lattice planes sharing the viewing direction $\mathrm{MT}[112]$ $\|$ $\mathrm{PL}[5\bar{1}8]$ as their common zone axis are perfectly coherent across a magnetite–plagioclase interface that is parallel to $\mathrm{MT}(1\bar{1}0)$ and $\mathrm{PL}(150)$. Such a situation has been referred to as an *exact phase boundary* by Robinson et al. (1971, 1977) and Fleet (1982) and corresponds to an O-line in O-lattice theory (Luo & Weatherly, 1987; Bollmann, 2012). In addition, a best fit direction lies in the $\mathrm{MT}(2\bar{2}0)$ $\|$ $\mathrm{PL}(150)$ lattice planes, which makes these lattice planes prone to serve as the habit plane for the growth of plate-shaped magnetite. The basal plane of the plate-shaped inclusion thus corresponds to an exact boundary for all lattice planes pertaining to this zone. This condition may, but need not necessarily produce a plate-shaped magnetite inclusion. Needle-shaped inclusions with this COR are also observed. For example, the cross-section of the $\mathrm{PL}(\bar{3}12)$n-MT micro-inclusion in main orientation containing interface segment $\mathrm{MT}(20\bar{2})$ $\|$ $\mathrm{PL}(150)$ corresponds to the above-mentioned $\mathrm{MT}(2\bar{2}0)$ $\|$ $\mathrm{PL}(150)$ alignment.

The analysis of the $\Delta\boldsymbol{g}$ vectors connecting lattice planes in constrained magnetite with those in unconstrained plagioclase must be considered as a thought experiment. It is not clear, whether the lattice planes sharing the $\mathrm{MT}[112]$ $\|$ $\mathrm{PL}[5\bar{1}8]$ directions as their common zone axis were coherent across the magnetite–plagioclase interface at any time. As a matter of fact, such coherency would require that either one or both of the lattices were substantially deformed with associated elastic strain energy. The lattice misfit between magnetite and plagioclase in the actual configuration must be accommodated by atomic interfacial steps and dislocations (Ye & Zhang, 2002). Generally, in the actual configuration the interface consists of the habit plane as derived from the CCSL method, which decomposes into an arrangement of terraces and steps that accommodate the misfit (Howe & Spanos, 1999; Ye & Zhang, 2002; Shi et al., 2013). The exact nature of the dislocations at the magnetite–plagioclase interface remain unclear. Nevertheless, the analysis is considered instructive for interpreting the actually observed COR and lattice match, which only slightly deviate from the fully coherent interface between constrained magnetite and unconstrained plagioclase.

The plate-shaped magnetite micro-inclusions are often located in plagioclase domains that are devoid of needle-shaped inclusions (Fig. 1). It may thus be hypothesised that the plate-shaped magnetite micro-inclusions were formed by recrystallisation of several needle-shaped magnetite inclusions into the energetically more favourable plate morphology.

SUMMARY AND CONCLUSIONS

The crystallographic basis of the SORs and CORs between needle-, lath- and plate-shaped magnetite micro-inclusions and plagioclase host was investigated using correlated optical and scanning transmission electron microscopy. The magnetite–plagioclase interfaces are crystalline, with no amorphous layer

or gap between the two phases. The magnetite micro-inclusions of the plane normal type are elongated parallel to one of their MT<111> directions, which, in turn, is perpendicular to one of seven specific plagioclase lattice planes including PL(112), PL($\bar{3}$12), PL(150), PL(1$\bar{5}$0), PL(100), PL($\bar{3}$12) and PL(1$\bar{1}$2) defining seven orientation classes. The inclusions elongation direction and shape orientations confer to the parallel alignment of the MT{222} lattice planes with either one of these specific lattice planes of plagioclase. This is ascribed to the good match between oxygen layers in the magnetite and plagioclase crystal structures across magnetite–plagioclase interfaces bounding the magnetite inclusions parallel to their elongation direction, which is ensured for these orientation relationships.

For each orientation class, specific orientation variants characterised by at least one additional parallel alignment of crystallographic planes or directions between magnetite and plagioclase are observed. When the additional alignment is PL[14, −10, 7] ∥ MT[100], the inclusion is classified as being in nucleation orientation, where FeO_6 octahedra of magnetite fit into channels parallel to PL[001] in the crystal structure of plagioclase in a favourable manner. The inclusions in nucleation orientation have regular, mostly MT{220} faceted cross-sections. The facets are mainly controlled by low index lattice planes of magnetite and by the commensurate impingement of low index magnetite and plagioclase lattice planes along the interface. Moreover, the inclusions in nucleation orientation typically show exact alignment of their elongation direction to the respective plane-normal direction. If, in addition to the MT{111} ∥ PL(*hkl*) alignment, one of the MT{220} lattice planes is parallel to another one of the specific plagioclase lattice planes, the inclusion is classified as being in main orientation. These inclusions show more complex cross-sections with typically only two facet orientations and otherwise curved, locally re-entrant magnetite–plagioclase interface segments. The facets of magnetite micro-inclusions in main orientation are mainly controlled by the parallel alignment of low index lattice planes of both, magnetite and plagioclase, and the inclusion elongation direction deviates by up to about 5° from the respective PL(*hkl*)-n direction.

The oxygen sub-lattices of magnetite and plagioclase are suggested to be responsible for the preferred orientation relationships as the observed CORs and SORs ensure continuity of the oxygen sub-lattices across the magnetite–plagioclase interfaces. In addition, the observed CORs and SORs minimises the re-arrangement of oxygen atoms during growth of magnetite inside plagioclase.

The morphologies of the magnetite micro-inclusions indicate a potential transformation from nucleation to main orientations, an evolution that may be important in the context of paleomagnetic reconstructions relying on the natural remanent magnetisation of single grains of magnetite bearing plagioclase. Oriented magnetite micro-inclusions in plagioclase are common in mafic intrusive rocks from a variety of geological settings. Our findings from ocean floor gabbros are likely transferable to these other occurrences.

FUNDING

DATA AVAILABILITY

The data underlying this article are available in the article and in its online supplementary materials.

CONFLICT OF INTEREST

All authors have seen and agree with the contents of the manuscript and there is no financial interest. The authors have no conflict of interest to declare.

ACKNOWLEDGEMENT

References

Ageeva, O., Habler, G., Topa, D., Waitz, T., Li, C., Pertsev, A., Griffiths, T., Zhilicheva, O. & Abart, R. (2016). Plagioclase hosted Fe-Ti-oxide micro-inclusions in an oceanic gabbro-plagiogranite association from the mid Atlantic ridge at 13°34' N. *American Journal of Science* **316**(2), 85–109. https://doi.org/10.2475/02.2016.01.

Ageeva, O., Habler, G., Pertsev, A. & Abart, R. (2017). Fe-Ti oxide micro-inclusions in clinopyroxene of oceanic gabbro: phase content, orientation relations and petrogenetic implication. *Lithos* **290-291**, 104–115. https://doi.org/10.1016/j.lithos.2017.08.007.

Ageeva, O., Bian, G., Habler, G., Pertsev, A. & Abart, R. (2020). Crystallographic and shape orientations of magnetite micro-inclusions in plagioclase. *Contributions to Mineralogy and Petrology* **175**(10), 95. https://doi.org/10.1007/s00410-020-01735-8.

Ageeva, O., Habler, G., Gilder, S. A., Schuster, R., Pertsev, A., Pilipenko, O., Bian, G. & Abart, R. (2022). Oriented magnetite inclusions in plagioclase: implications for the anisotropy of magnetic remanence. *Geochemistry, Geophysics, Geosystems* **23**(2), e2021GC010272. https://doi.org/10.1029/2021GC010272.

Beltenev, V., Ivanov, V., Rozhdestvenskaya, I., Cherkashov, G., Stepanova, T., Shilov, V., Pertsev, A., Davydov, M., Egorov, I., Melekestseva, I., Narkevsky, E. & Ignatov, V. (2007). A new hydrothermal field at 13°30' N on the mid-Atlantic ridge. *Inter-Ridge News* **16**(9), 9–10.

Beltenev, V. E., Ivanov, I., Rozhdestvenskaya, I., Cherkashev, G. A., Stepanova, T. V., Shilov, V. V., Davydov, M. P., Laiba, A. A., Kaylio, V., Narkevsky, E., Pertsev, A. N., Dobretzova, I., Gustaytis, A., Ye, P., Amplieva, E. E., Evrard, C., Moskalev, L. I. & Gebruk, A. V. (2009). New data about hydrothermal fields on the mid-Atlantic ridge between 11°-14°N: 32nd cruise of R/V professor Logatchev. *InterRidge News* **18**, 13–17.

Bian, G., Ageeva, O., Rečnik, A., Habler, G. & Abart, R. (2021). Formation pathways of oriented magnetite micro-inclusions in plagioclase from oceanic gabbro. *Contributions to Mineralogy and Petrology* **176**(12), 104. https://doi.org/10.1007/s00410-021-01864-8.

Bollmann, W. (2012) *Crystal Defects and Crystalline Interfaces*. Berlin/Heidelberg, Germany: Springer Science & Business Media.

Bosch, E. G. T. & Lazić, I. (2015). Analysis of HR-STEM theory for thin specimen. *Ultramicroscopy* **156**, 59–72. https://doi.org/10.1016/j.ultramic.2015.02.004.

Brown, W. L., Openshaw, R. E., McMillan, P. F. & Henderson, C. M. B. (1984). A review of the expansion behavior of alkali feldspars:

coupled variations in cell parameters and possible phase transitions. *American Mineralogist* **69**(11–12), 1058–1071.

Champness, P. E. (1970). Nucleation and growth of iron oxides in olivines, (mg,Fe)2SiO4. *Mineralogical Magazine* **37**(291), 790–800. https://doi.org/10.1180/minmag.1970.037.291.05.

Christian, J. W. (2002) *The Theory of Transformations in Metals and Alloys*. Oxford, UK: Newnes.

Cipriani, A., Bonatti, E., Brunelli, D. & Ligi, M. (2009). 26 million years of mantle upwelling below a segment of the mid Atlantic ridge: the Vema lithospheric section revisited. *Earth and Planetary Science Letters* **285**(1), 87–95. https://doi.org/10.1016/j.epsl.2009.05.046.

Dahmen, U. (1982). Orientation relationships in precipitation systems. *Acta Metallurgica* **30**(1), 63–73. https://doi.org/10.1016/0001-6160(82)90045-1.

Dahmen, U., Ferguson, P. & Westmacott, K. H. (1984). Invariant line strain and needle-precipitate growth directions in Fe-cu. *Acta Metallurgica* **32**(5), 803–810. https://doi.org/10.1016/0001-6160(84)90153-6.

Dunlop, D. J. & Özdemir, Ö. (2001) *Rock Magnetism: Fundamentals and Frontiers*. Cambridge, England: Cambridge University Press.

Escartín, J., Mével, C., Petersen, S., Bonnemains, D., Cannat, M., Andreani, M., Augustin, N., Bezos, A., Chavagnac, V., Choi, Y., Godard, M., Haaga, K., Hamelin, C., Ildefonse, B., Jamieson, J., John, B., Leleu, T., MacLeod, C. J., Massot-Campos, M. & Garcia, R. (2017). Tectonic structure, evolution, and the nature of oceanic core complexes and their detachment fault zones (13°20′N and 13°30′N, mid Atlantic ridge). *Geochemistry, Geophysics, Geosystems* **18**(4), 1451–1482. https://doi.org/10.1002/2016GC006775.

Feinberg, J. M., Wenk, H.-R., Renne, P. R. & Scott, G. R. (2004). Epitaxial relationships of clinopyroxene-hosted magnetite determined using electron backscatter diffraction (EBSD) technique. *American Mineralogist* **89**(2–3), 462–466. https://doi.org/10.2138/am-2004-2-328.

Fleet, M. E. (1981). The structure of magnetite. *Acta Crystallographica Section B: Structural Crystallography and Crystal Chemistry* **37**(4), 917–920. https://doi.org/10.1107/S0567740881004597.

Fleet, M. E. (1982). Orientation of phase and domain boundaries in crystalline solids. *American Mineralogist* **67**(9–10), 926–936.

Fleet, M. E., Bilcox, G. A. & Barnett, R. L. (1980). Oriented magnetite inclusions in pyroxenes from the Grenville province. *The Canadian Mineralogist* **18**(1), 89–99.

Gao, W., Ciobanu, C., Cook, N., Slattery, A., Huang, F. & Wang, D. (2019). Nanoscale study of lamellar exsolutions in clinopyroxene from olivine gabbro: recording crystallization sequences in iron-rich layered intrusions. *American Mineralogist* **104**(2), 244–261. https://doi.org/10.2138/am-2019-6764.

Howe, J. M. (1997) *Interfaces in Materials: Atomic Structure, Thermodynamics and Kinetics of Solid-Vapor, Solid-Liquid and Solid-Solid Interfaces*. Hoboken, New Jersey: Wiley.

Howe, J. M. & Spanos, G. (1999). Atomic structure of the austenite-cementite interface of proeutectoid cementite plates. *Philosophical Magazine A* **79**(1), 9–30. https://doi.org/10.1080/01418619908214271.

Howe, J. M., Reynolds, W. T. & Vasudevan, V. K. (2002). Static and in-situ high-resolution transmission electron microscopy investigations of the atomic structure and dynamics of massive transformation interfaces in a Ti-Al alloy. *Metallurgical and Materials Transactions A* **33**(8), 2391–2411. https://doi.org/10.1007/s11661-002-0362-4.

Hwang, S.-L., Shen, P., Yui, T.-F. & Chu, H.-T. (2010). On the coherency-controlled growth habit of precipitates in minerals. *Journal of Applied Crystallography* **43**, 417–428. https://doi.org/10.1107/S0021889810007454.

Karson, J. A., & Lawrence, R. M. (1997). Tectonic setting of serpentinite exposures on the western median valley wall of the MARK area in the vicinity of Site 920. In *Proceedings-Ocean Drilling Program Scientific Results*, Vol. **153**. National Science Foundation, pp. 5–22. https://doi.org/10.2973/odp.proc.sr.153.1997

Lazić, I., Bosch, E. G. T. & Lazar, S. (2016). Phase contrast STEM for thin samples: integrated differential phase contrast. *Ultramicroscopy* **160**, 265–280. https://doi.org/10.1016/j.ultramic.2015.10.011.

Levy, D., Giustetto, R. & Hoser, A. (2012). Structure of magnetite (Fe3O4) above the curie temperature: a cation ordering study. *Physics and Chemistry of Minerals* **39**(2), 169–176. https://doi.org/10.1007/s00269-011-0472-x.

Luo, C. P. & Weatherly, G. C. (1987). The invariant line and precipitation in a Ni-45 wt% Cr alloy. *Acta Metallurgica* **35**(8), 1963–1972. https://doi.org/10.1016/0001-6160(87)90025-3.

MacLeod, C. J., Searle, R. C., Murton, B. J., Casey, J. F., Mallows, C., Unsworth, S. C., Achenbach, K. L. & Harris, M. (2009). Life cycle of oceanic core complexes. *Earth and Planetary Science Letters* **287**(3), 333–344. https://doi.org/10.1016/j.epsl.2009.08.016.

Nikolaisen, E. S., Harrison, R. J., Fabian, K. & McEnroe, S. A. (2020). Hysteresis of natural magnetite ensembles: micromagnetics of silicate-hosted magnetite inclusions based on focused-ion-beam Nanotomography. *Geochemistry, Geophysics, Geosystems* **21**(11), e2020GC009389. https://doi.org/10.1029/2020GC009389.

Nikolaisen, E. S., Harrison, R., Fabian, K., Church, N., McEnroe, S. A., Sørensen, B. E. & Tegner, C. (2022). Hysteresis parameters and magnetic anisotropy of silicate-hosted magnetite exsolutions. *Geophysical Journal International* **229**(3), 1695–1717. https://doi.org/10.1093/gji/ggac007.

Ondréas, H., Cannat, M., Fouquet, Y. & Normand, A. (2012). Geological context and vents morphology of the ultramafic-hosted Ashadze hydrothermal areas (mid-Atlantic ridge 13°N). *Geochemistry, Geophysics, Geosystems* **13**(11). https://doi.org/10.1029/2012GC004433.

Pertsev, A. N., Bortnikov, N. S., Vlasov, E. A., Beltenev, V. E., Dobretsova, I. G. & Ageeva, O. A. (2012). Recent massive sulfide deposits of the Semenov ore district, mid-Atlantic ridge, 13°31′ N: associated rocks of the oceanic core complex and their hydrothermal alteration. *Geology of Ore Deposits* **54**(5), 334–346. https://doi.org/10.1134/S1075701512050030.

Robinson, P., Jaffe, H. W., Ross, M. & Klein, C., Jr. (1971). Orientation of Exsolution lamellae in Clinopyroxenes and Clinoamphiboles: consideration of optimal phase boundaries. *American Mineralogist* **56**(5–6), 909–939.

Robinson, P., Ross, M., Nord, G. L., Smyth, J. R. & Jaffe, H. W. (1977). Exsolution lamellae in augite and pigeonite; fossil indicators of lattice parameters at high temperature and pressure. *American Mineralogist* **62**(9–10), 857–873.

Shi, Z.-Z., Dai, F.-Z., Zhang, M., Gu, X.-F. & Zhang, W.-Z. (2013). Secondary coincidence site lattice model for truncated triangular β-Mg2Sn precipitates in a mg-Sn-based alloy. *Metallurgical and Materials Transactions A* **44**(6), 2478–2486. https://doi.org/10.1007/s11661-013-1633-y.

Sobolev, P. O. (1990). Orientation of acicular iron-ore mineral inclusions in plagioclase. *International Geology Review* **32**(6), 616–628. https://doi.org/10.1080/00206819009465804.

Sutton, A. P. & Balluffi, R. W. (1995) *Interfaces in crystalline materials*. Oxford, England: Clarendon Press; Oxford University Press.

Tan, W., Liu, P., He, H., Wang, C. Y. & Liang, X. (2016). Mineralogy and origin of Exsolution in Ti-rich magnetite from different magmatic Fe-ti oxide-bearing intrusions. *Canadian Mineralogist* **54**, 539–553. https://doi.org/10.3749/canmin.1400069.

Tan, W., Wang, C., Reddy, S., He, H., Xian, H. & Xing, C. (2022). Magnetite-rutile symplectite in ilmenite records magma

hydration in layered intrusions. *American Mineralogist* **107**(3), 395–404. https://doi.org/10.2138/am-2021-7777.

Tarduno, J. A., Cottrell, R. D. & Smirnov, A. V. (2006). The paleomagnetism of single silicate crystals: recording geomagnetic field strength during mixed polarity intervals, superchrons, and inner core growth. *Reviews of Geophysics* **44**(1). https://doi.org/10.1029/2005RG000189.

Tribaudino, M., Angel, R. J., Cámara, F., Nestola, F., Pasqual, D. & Margiolaki, I. (2010). Thermal expansion of plagioclase feldspars. *Contributions to Mineralogy and Petrology* **160**(6), 899–908. https://doi.org/10.1007/s00410-010-0513-3.

Wayman, C. M. (1994). The phenomenological theory of martensite crystallography: interrelationships. *Metallurgical and Materials Transactions A* **25**(9), 1787–1795. https://doi.org/10.1007/BF02649029.

Weatherly, G. C. & Nicholson, R. B. (1968). An electron microscope investigation of the interfacial structure of semi-coherent precipitates. *The Philosophical Magazine: A Journal of Theoretical Experimental and Applied Physics* **17**(148), 801–831. https://doi.org/10.1080/14786436808223031.

Wenk, H. R., Joswig, W., Tagai, T., Korekawa, M. & Smith, B. K. (1980). The average structure of an 62–66 labradorite. *American Mineralogist* **65**(1–2), 81–95.

Wenk, H.-R., Chen, K. & Smith, R. (2011). Morphology and microstructure of magnetite and ilmenite inclusions in plagioclase from Adirondack anorthositic gneiss. *American Mineralogist* **96**(8–9), 1316–1324. https://doi.org/10.2138/am.2011.3760.

Ye, F. & Zhang, W.-Z. (2002). Coincidence structures of interfacial steps and secondary misfit dislocations in the habit plane between Widmanstätten cementite and austenite. *Acta Materialia* **50**(11), 2761–2777. https://doi.org/10.1016/S1359-6454(02)00077-0.

Yücelen, E., Lazić, I. & Bosch, E. G. T. (2018). Phase contrast scanning transmission electron microscopy imaging of light and heavy atoms at the limit of contrast and resolution. *Scientific Reports* **8**, 2676. https://doi.org/10.1038/s41598-018-20377-2.

Zhang, W.-Z. (2020). Reproducible orientation relationships developed from phase transformations—role of interfaces. *Crystals* **10**(11), 1042. https://doi.org/10.3390/cryst10111042.

Zhang, W.-Z. & Purdy, G. R. (1993). O-lattice analyses of interfacial misfit. I. General considerations. *Philosophical Magazine A* **68**(2), 279–290. https://doi.org/10.1080/01418619308221205.

Zhang, R. Y., Shu, J. F., Mao, H. K. & Liou, J. G. (1999). Magnetite lamellae in olivine and clinohumite from Dabie UHP ultramafic rocks, Central China. *American Mineralogist* **84**(4), 564–569. https://doi.org/10.2138/am-1999-0410.

Zhang, W.-Z., Ye, F., Zhang, C., Qi, Y. & Fang, H.-S. (2000). Unified rationalization of the Pitsch and T–H orientation relationships between Widmanstätten cementite and austenite. *Acta Materialia* **48**(9), 2209–2219. https://doi.org/10.1016/S1359-6454(00)00033-1.

APPENDIX

Two pairs of diffraction spots, each comprising two closely spaced diffraction spots one pertaining to plagioclase and the other pertaining to magnetite, were selected, and a transformation was applied on magnetite to make the selected nearly coincident diffraction spots coincide. The transformation is represented by transformation matrix $\boldsymbol{A}_p$ in direct space and by transformation matrix $\boldsymbol{A}_p^*$ in reciprocal space. The transformation matrix is obtained in two steps: In the first step, the magnetite and plagioclase unit cells are expressed in terms of a common orthonormal

coordinate system $Oxyz$ with unit vectors along the Ox, Oy and Oz-axes defining the base vectors $\mathbf{i}$, $\mathbf{j}$ and $\mathbf{k}$. The unit cell of a crystal is usually expressed in the crystal coordinate system defined by the lattice constants $a, b, c, \alpha, \beta, \gamma$ with the base vector $\mathbf{a}$, $\mathbf{b}$ and $\mathbf{c}$. The orientation of the crystal coordinate system in the orthonormal coordinate system is chosen so that $\mathbf{a} \parallel Ox$ and $\mathbf{a} \times \mathbf{c} \parallel Oy$. The base vectors of the crystal coordinate system $\mathbf{a}$, $\mathbf{b}$ and $\mathbf{c}$ expressed in orthonormal coordinates read

$$\boldsymbol{a} = \mathbf{i}s_1^1 + \mathbf{j}s_1^2 + \mathbf{k}s_1^3$$
$$\boldsymbol{b} = \mathbf{i}s_2^1 + \mathbf{j}s_2^2 + \mathbf{k}s_2^3$$
$$\boldsymbol{c} = \mathbf{i}s_3^1 + \mathbf{j}s_3^2 + \mathbf{k}s_3^3$$

In matrix notation this is

$$\boldsymbol{u}^T = \boldsymbol{u}_{(orth)}^T \mathbf{S}$$

where

$$\mathbf{S} = \begin{pmatrix} s_1^1 & s_2^1 & s_3^1 \\ s_1^2 & s_2^2 & s_3^2 \\ s_1^3 & s_2^3 & s_3^3 \end{pmatrix}$$

$\mathbf{u}$ and $\mathbf{u}_{(orth)}$ represent the base vectors of the crystal coordinate system and of the orthonormal coordinate system, respectively, and $|^T$ is the transpose.

The elements of the $\mathbf{S}$ matrix are obtained from the scalar products of the base vectors in crystal coordinate making use of the orthogonality of the base vectors in the orthonormal coordinate system (Bollmann, 2012), which yields

$$\mathbf{S} = \begin{pmatrix} a & b \bullet \cos\gamma & c \bullet \cos\beta \\ 0 & (b/\sin\beta)\left(\sin^2\beta - \cos^2\beta - \cos^2\gamma + \cos\alpha \bullet \cos\beta \bullet \cos\gamma\right)^{1/2} & 0 \\ 0 & (b/\sin\beta)\,(\cos\alpha - \cos\beta \bullet \cos\gamma) & c \bullet \sin\beta \end{pmatrix}$$

The column vectors of the $\mathbf{S}$ matrix are the unit vectors in the crystal coordinate system expressed as linear combinations of the base vectors of the orthonormal coordinate system.

The lattice constants of cubic magnetite $a_{MT} = 8.397$ Å and of triclinic plagioclase $a_{PL} = 8.1736$ Å, $b_{PL} = 12.8736$ Å, $c_{PL} = 7.1022$ Å, $\alpha_{PL} = 93.462°$, $\beta_{PL} = 116.054°$, $\gamma_{PL} = 90.475°$, taken from Fleet (1981) and Wenk et al. (1980), respectively, were used to obtain $\mathbf{S}_{MT}$ and $\mathbf{S}_{PL}$ based on the above equation. Given a column vector $\mathbf{v}$ in the crystal coordinate system, the corresponding vector in the orthonormal coordinate system $\mathbf{v}_{(orth)}$ can be expressed as $\mathbf{v}_{(orth)} = \mathbf{S}\mathbf{v}$.

In the next step, the transformation matrix $\boldsymbol{A}_p^*$ is applied to magnetite to make the selected pairs of diffraction spots, which are represented by the reciprocal lattice vectors $\boldsymbol{g}_{PL1}$, $\boldsymbol{g}_{PL2}$, $\boldsymbol{g}_{PL3}$ and $\boldsymbol{g}_{MT1}$, $\boldsymbol{g}_{MT2}$, $\boldsymbol{g}_{MT3}$, respectively, coincide. The transformation matrix $\boldsymbol{A}_p^*$ must suffice the condition

$$\boldsymbol{A}_p^* \bullet \left(\mathbf{S}_{MT}^* \bullet \boldsymbol{G}_{MT}\right) = \mathbf{S}_{PL}^* \bullet \boldsymbol{G}_{PL}$$

where $\boldsymbol{A}_p^*$ is the $\boldsymbol{A}_p$ in reciprocal space $\boldsymbol{A}_p^* = \left(\boldsymbol{A}_p^T\right)^{-1}$, $\mathbf{S}_{MT}^*$ and $\mathbf{S}_{PL}^*$ are $\mathbf{S}_{MT}$ and $\mathbf{S}_{PL}$ expressed in reciprocal space, $\boldsymbol{G}_{PL}$ is a 3×3 matrix $\boldsymbol{G}_{PL} = \left(\boldsymbol{g}_{PL1}, \boldsymbol{g}_{PL2}, \boldsymbol{g}_{PL3}\right)$, where

$$\boldsymbol{g}_{PL1} = \begin{pmatrix} -3 \\ 1 \\ 2 \end{pmatrix}, \boldsymbol{g}_{PL2} = \begin{pmatrix} 2 \\ 10 \\ 0 \end{pmatrix}, \boldsymbol{g}_{PL3} = \begin{pmatrix} 0.465 \\ -0.761 \\ 1 \end{pmatrix}/2$$

The third vector $\boldsymbol{g}_{PL3}$ is equivalent to PL[5$\bar{1}$8]/5 in reciprocal space. It is obtained by the following method: (i) PL[5$\bar{1}$8] is transformed into a vector in reciprocal space preserving the same direction, i.e. PL[5$\bar{1}$8] = PL(0.465, −0.761,1); (ii) the reciprocal vector

PL(0.465, −0.761,1) is divided by 2 to adjust the length of PL[$5\bar{1}8$]/5. $\mathbf{G}_{MT}$, is a 3×3 matrix $\mathbf{G}_{MT} = (\boldsymbol{g}_{MT1}, \boldsymbol{g}_{MT2}, \boldsymbol{g}_{MT3})$, with

$$\boldsymbol{g}_{MT1} = \begin{pmatrix} 2 \\ 2 \\ -2 \end{pmatrix}, \boldsymbol{g}_{MT2} = \begin{pmatrix} 5 \\ -5 \\ 0 \end{pmatrix}, \boldsymbol{g}_{MT3} = \begin{pmatrix} 1 \\ 1 \\ 2 \end{pmatrix} /3$$

The third vector $\boldsymbol{g}_{MT3}$ is equivalent to MT[112]/2 in reciprocal space.

In reciprocal space the constraint is obtained by rearranging the above equation, which yields

$$\mathbf{A}_p^* = \boldsymbol{S}_{PL}^* \bullet \mathbf{G}_{PL} \bullet (\mathbf{S}_{MT}^* \bullet \mathbf{G}_{MT})^{-1}$$

and finally, $\mathbf{A}_p$ is obtained from $\mathbf{A}_p = \left((\mathbf{A}_p^*)^{-1}\right)^T$, which yields

$$\mathbf{A}_p = \begin{pmatrix} -0.2339 & -0.6241 & 0.7733 \\ 0.7240 & -0.6319 & -0.3220 \\ 0.6814 & 0.4666 & 0.5428 \end{pmatrix}$$

The constrained MT unit cell MT^c can be expressed in orthonormal coordinate as

$$\mathbf{S}_{MT}^c = \mathbf{A}_p \bullet \mathbf{S}_{MT}$$

which yields

$$\mathbf{S}_{MT}^c = \begin{pmatrix} -1.9635 & -5.2387 & 6.4911 \\ 6.0768 & -5.3046 & -2.7030 \\ 5.7195 & 3.9168 & 4.5561 \end{pmatrix}$$

The transformation applied to magnetite does not change the translation vectors of the unit cell, thus the constrained lattice constants, as well as the angles between each unit vector can be calculated from $\mathbf{S}_{MT}^c$. For instance, the constrained base vector $\boldsymbol{a}_{MT}^c$ can be expressed in orthonormal coordinate $\boldsymbol{a}_{MT}^c = \mathbf{S}_{MT}^c \bullet [100]'$, that is the first column in $\mathbf{S}_{MT}^c$. The value of the base vector $\boldsymbol{a}_{MT}^c = 8.5730$ Å is the new lattice constant of the constrained magnetite. Similarly, $\boldsymbol{b}_{MT}^c$ and $\boldsymbol{c}_{MT}^c$ can be derived in the same manner. The angle between the base vectors $\boldsymbol{b}_{MT}^c$ and $\boldsymbol{c}_{MT}^c$ of the constrained magnetite thus define the angle $\boldsymbol{\alpha}_{MT}^c = \measuredangle (\boldsymbol{b}_{MT}^c, \boldsymbol{c}_{MT}^c)$, and is derived by the inverse tangent formula $\boldsymbol{\alpha}_{MT}^c = atan2(\,|\,\|\boldsymbol{b}_{MT}^c \times \boldsymbol{c}_{MT}^c\|, \boldsymbol{b}_{MT}^c \bullet \boldsymbol{c}_{MT}^c)$. $\boldsymbol{\beta}_{MT}^c$ and $\boldsymbol{\gamma}_{MT}^c$ can be obtained following the same procedure. The resulting lattice constants of constrained magnetite MT^c are listed in Table 4.